Geochimica et Cosmochimica Acta 335 (2022) 68–84

Contents lists available at ScienceDirect

Geochimica et Cosmochimica Acta

journal homepage: www.elsevier.com/locate/gca

Nitrogen, helium, and argon reveal the magmatic signature of fumarole gases and episodes of outgassing from upper-crustal magma reservoirs: The case of the Nisyros caldera (Aegean Arc, Greece)

Giulio Bini [a,b,*], Giovanni Chiodini [b], Stefano Caliro [c], Franco Tassi [d,e], Orlando Vaselli [d,e], Andrea L. Rizzo [f,g], Silvio Mollo [h,i], Georgios E. Vougioukalakis [l], Olivier Bachmann [a]

[a] Institute of Geochemistry and Petrology, ETH Zürich, Clausiusstrasse 25, 8092 Zürich, Switzerland
[b] Istituto Nazionale di Geofisica e Vulcanologia, Sezione di Bologna, Via Creti 12, 40128 Bologna, Italy
[c] Istituto Nazionale di Geofisica e Vulcanologia, Osservatorio Vesuviano, Sezione di Napoli, Via Diocleziano 328, 80125 Napoli, Italy
[d] Department of Earth Sciences, University of Florence, Via G. La Pira 4, 50121 Firenze, Italy
[e] Institute of Geosciences and Earth Resources (IGG), National Research Council of Italy (CNR), Via G. La Pira 4, 50121 Firenze, Italy
[f] Istituto Nazionale di Geofisica e Vulcanologia, Sezione di Palermo, Via Ugo La Malfa 153, 90146 Palermo, Italy
[g] Istituto Nazionale di Geofisica e Vulcanologia, Sezione di Milano, Via Alfonso Corti 12, 20133 Milano, Italy
[h] Department of Earth Sciences, Sapienza University of Rome, 00185 Rome, Italy
[i] Istituto Nazionale di Geofisica e Vulcanologia, Sezione di Roma 1, Via di Vigna Murata 605, 00143 Roma, Italy
[l] Department of Natural and Technological Hazards, Hellenic Survey of Geology and Mineral Exploration, S. Lui 1, Olympic Village, 13677 Aharne, Athens, Greece

ARTICLE INFO

Article history:
Received 19 April 2022
Accepted 23 August 2022
Available online 29 August 2022
Associate editor: Manuel Moreira

Keywords:
Noble gases
Nitrogen isotope
Mixing modeling
Magmatic degassing
High-crystallinity mush
Caldera
Unrest
CO_2

ABSTRACT

The chemical composition of gases emitted by active volcanoes reflects both magma degassing and shallower processes, such as fluid-rock hydrothermal interaction and mixing with atmospheric-derived fluids. Untangling the magmatic fluid endmember within surface gas emission is therefore challenging, even with the use of well-known magma degassing tracers such as noble gases. Here, we investigate the deep magmatic fluid composition at the Nisyros caldera (Aegean Arc, Greece) by measuring nitrogen and noble gas abundances and isotopes in naturally degassing fumaroles. Gas samples were collected from 32 fumarolic vents at water-boiling temperature between 2018 and 2021. These fumaroles are admixtures of magmatic fluids typical of subduction zones, groundwater (or air saturated water, ASW), and air. The N_2, He, and Ar composition of the magmatic endmember is calculated by reverse mixing modeling and shows $N_2/He = 31.8 \pm 4.5$, $N_2/Ar = 281.6$, $\delta^{15}N = +7 \pm 3$ ‰, $^3He/^4He = 6.2$ Ra (where Ra is air $^3He/^4He$), and $^{40}Ar/^{36}Ar = 551.6 \pm 19.8$. Although N_2/He is significantly low with respect to typical values for arc volcanoes (1,000–10,000), the contribution of subducted sediments to the Aegean Arc magma generation is reflected by the positive $\delta^{15}N$ values of Nisyros fumaroles. The low N_2/He ratio indicates N_2-depletion due to solubility-controlled differential degassing of an upper-crustal silicic (dacitic/rhyodacitic) melt in a high-crystallinity reservoir. We compare our 2018–2021 data with N_2, He, and Ar values collected from the same fumaroles during a hydrothermal unrest following the seismic crisis in 1996–1997. Results show additions of both magmatic fluid and ASW during this unrest. In the same period, fumarolic vents display an increase in magmatic species relative to hydrothermal gas, such as CO_2/CH_4 and He/CH_4 ratios, an increase of ~50 °C in the equilibrium temperature of the hydrothermal system (up to 325 °C), and greater amounts of vapor separation. These variations reflect an episode of magmatic fluid expulsion during the seismic crisis. The excess of heat and mass supplied by the magmatic fluid injection is then dissipated through boiling of deeper and peripheral parts of the hydrothermal system. Reverse mixing modeling of fumarolic N_2-He-Ar has therefore important ramifications not only to disentangle the magmatic signature from gases emitted during periods of dormancy, but also to trace episodes of magmatic outgassing and better understand the state of the upper crustal reservoir.

* Corresponding author at: Institute of Geochemistry and Petrology, ETH Zürich, Clausiusstrasse 25, 8092 Zürich, Switzerland.
E-mail address: giulio.bini@ingv.it (G. Bini).

https://doi.org/10.1016/j.gca.2022.08.028
0016-7037/

1. Introduction

Monitoring surface gas emissions from active volcanoes has important implications for volcanic surveillance and for a better understanding of subsurface processes. Volcanoes emit many gaseous chemical species, and these reflect different fluid sources and complex physicochemical processes occurring in the Earth's mantle, crust, and atmosphere. Volatiles exsolve from silicate melts stored in magma chambers and are injected into overlying hydrothermal systems. These systems are characterized by convection of meteoric and magmatic water (Giggenbach, 1992) driven by heat transfer from magma chambers (Scott et al., 2015; Lamy-Chappuis et al., 2020). Here, magmatic fluids react with water and rocks before approaching the Earth's surface, losing some of their most acidic gases, such as SO_2, HCl, and HF, and producing more reduced species, such as CH_4 (Giggenbach, 1987; Chiodini, 2009). Consequently, the composition of the magmatic volatile phase can be significantly altered by the time it reaches the atmosphere.

Magmatic fluid expulsion during episodes of volcanic activity causes heating and pressure buildup in the overlying hydrothermal system, eventually triggering shallow seismicity (Chiodini et al., 2021). Overpressurization of the hydrothermal system can culminate in phreatic and phreatomagmatic eruptions and ultimately in magmatic eruptions (Rouwet et al., 2014). In some cases, these episodes of magmatic fluid expulsion are revealed by temporal variation in the chemistry of surface gas emissions. In particular, gases measured at the surface record an increase in the proportion of magmatic volatiles, such as CO_2 and He, relative to lower-temperature species typically produced in hydrothermal systems, such as CH_4 (Chiodini, 2009). For example, an increase in CO_2/CH_4 ratios measured in fumaroles was observed during the unrests of Mammoth Mountain (California, USA, in the 1990s; Sorey et al., 1998), Panarea (Italy, in the early 2000s; Chiodini et al., 2006), Mount Baker Volcano (Washington, USA, in 1975; Werner et al., 2009), Santorini (Greece, in 2011–2012; Tassi et al., 2013; Rizzo et al., 2015), Taal (Philippines, in 2011; Hernández et al., 2021), La Soufrière (Guadeloupe, French West Indies, in 2018; Moretti et al., 2020), and Campi Flegrei (Italy, in 2005–2014; Chiodini et al., 2015). Similar CO_2/CH_4 variations were also observed in the fumarolic vents of the Nisyros caldera, South Aegean Volcanic Arc (SAVA), Greece, after a seismic crisis recorded between 1996 and 1997 (Chiodini et al., 2002).

Variations in these reactive species may also be accompanied by changes in nitrogen and noble gas contents of surface gas emissions (e.g., Caracausi et al., 2003; Caliro et al., 2014; Rizzo et al., 2015). Due to their distinct isotope composition in mantle-derived fluids (e.g., $^3He/^4He$, $^{40}Ar/^{36}Ar$, and $\delta^{15}N$) relative to others Earth's reservoirs (crust, atmosphere, biosphere), and their relatively inert behavior, these species act as conservative tracers for magmatic fluids migrating towards the surface. However, they can mix with atmospheric components in the hydrothermal system, such as groundwater (or air saturated water, ASW) and air, making sometimes difficult the recognition of the original magmatic gas signature.

In this study, we use reverse mixing modeling (Albarède, 1995; Janoušek et al., 2016) of nitrogen and noble gas contents in Nisyros fumaroles to estimate the current composition of the magmatic volatile phase. Treating these gas emissions as admixtures of air, ASW, and an unknown magmatic endmember, enables us not only to disentangle the magmatic gas signature from Nisyros fluids but also to calculate the relative fraction of these three endmembers in each gas sample. Nitrogen isotopes are analyzed for the first time in these fluids, and together with those of He and Ar provide additional insights into the source of the magmatic volatiles currently outgassing from Nisyros and the state of its magma chamber. Finally, we compare the current reactive and nonreactive gas (N_2-He-Ar) data with those collected during the hydrothermal unrest that followed the 1996–1997 seismic crisis to evaluate the contribution of magmatic volatiles during such period of activity (Chiodini et al., 2002; Caliro et al., 2005). Together with variation in both the thermodynamic conditions of the hydrothermal system and CO_2/CH_4 and He/CH_4 ratios, N_2-He-Ar data shed light into an episode of magma outgassing during the seismic crisis.

2. Geologic setting

2.1. Volcanic and hydrothermal background

The Nisyros caldera is located in the easternmost part of the South Aegean Volcanic Arc (SAVA), which formed from the subduction of the African slab underneath the Aegean microplate (Fig. 1a). The SAVA consists of four major volcanic areas: Methana/Aegina, Milos, Santorini, and Kos-Nisyros-Gyali (Fig. 1a). Rollback and tearing of the African slab caused asthenospheric mantle flow in both the backarc extensional area of the Aegean Sea, towards the north of the SAVA, and western Anatolia, eastward of the SAVA (Jolivet et al., 2013; Klaver et al., 2016). Toroidal movements from this slab tear below western Anatolia might have driven the African subslab mantle to reach Nisyros and Santorini (Klaver et al., 2016). The accretionary prism of the Aegean subduction (the Mediterranean Ridge), extending towards south of the SAVA (Fig, 1a), is formed by stacks of sediments of the subducted Eastern Mediterranean Sea (the last remnant of the Tethys Ocean; Klaver et al., 2015). The composition of the sedimentary sequence predominantly consists of Sahara dust and Nile sediments and about 40–80 % of these are thought to be subducted rather than accreted (Kopf, 2003). The eastern part of the Mediterranean Ridge alternates Sahara dust, carbonate-rich pelagic marls, and smectite-rich turbidites of Nile provenance. Nevertheless, the sediment contributing to the current arc volcanism might mostly be dominated by a Nile-like component (Klaver et al., 2015).

Nisyros volcano presents an 8 km wide subaerial edifice (Fig. 1b), which is the result of numerous episodes of explosive and effusive eruptions occurred during the last 161 ky (Bachmann et al., 2012). The construction of Nisyros volcanic edifice started with a basaltic andesite seamount and gradually evolved in a subaerial cone by eruptions of more evolved magmas (Di Paola, 1974; Francalanci et al., 1995). Two 2–3 km^3 dense-rock equivalent Plinian eruptions (Lower and Upper Pumice) caused the collapse of the edifice about 60 ka (Popa et al., 2020) and the formation of a 3.8 km wide caldera in the center of the island (Fig. 1b; Bachmann et al., 2019). The youngest eruption (about 20 ka) consists in the extrusion of rhyodacitic lava domes (Postcaldera Domes) in the SW part of the island (Popa et al., 2020). The most recent activity on Nisyros was characterized by hydrothermal eruptions. The youngest explosions opened Polyvotis Mikros crater in 1887 and Polyvotis Megalos and Phlegethron craters during 1871–1873 (Fig. 1c; Marini et al., 1993 and references therein).

The southern part of the Nisyros caldera host an upflow zone of hydrothermal fluids, which are emitted into the atmosphere through NE-SW and NW-SE regional tectonic faults and hydrothermal craters (Fig. 1c; Caliro et al., 2005; Bini et al., 2019). Information about the hydrothermal system is given by both drilling of two geothermal wells (Nisyros-1 and Nisyros-2) in the caldera in the 1980s (Marini and Fiebig, 2005 and references therein) and the chemistry of surface fluid emissions, like fumaroles and thermal springs (Chiodini et al., 1993; Brombach et al., 2003; Fiebig et al., 2004; Marini and Fiebig, 2005). A high-enthalpy brine at about 340 °C is hosted in fractured diorites and thermometamorphic rocks at about 1.5 km depth. This fluid displays chloride concentra-

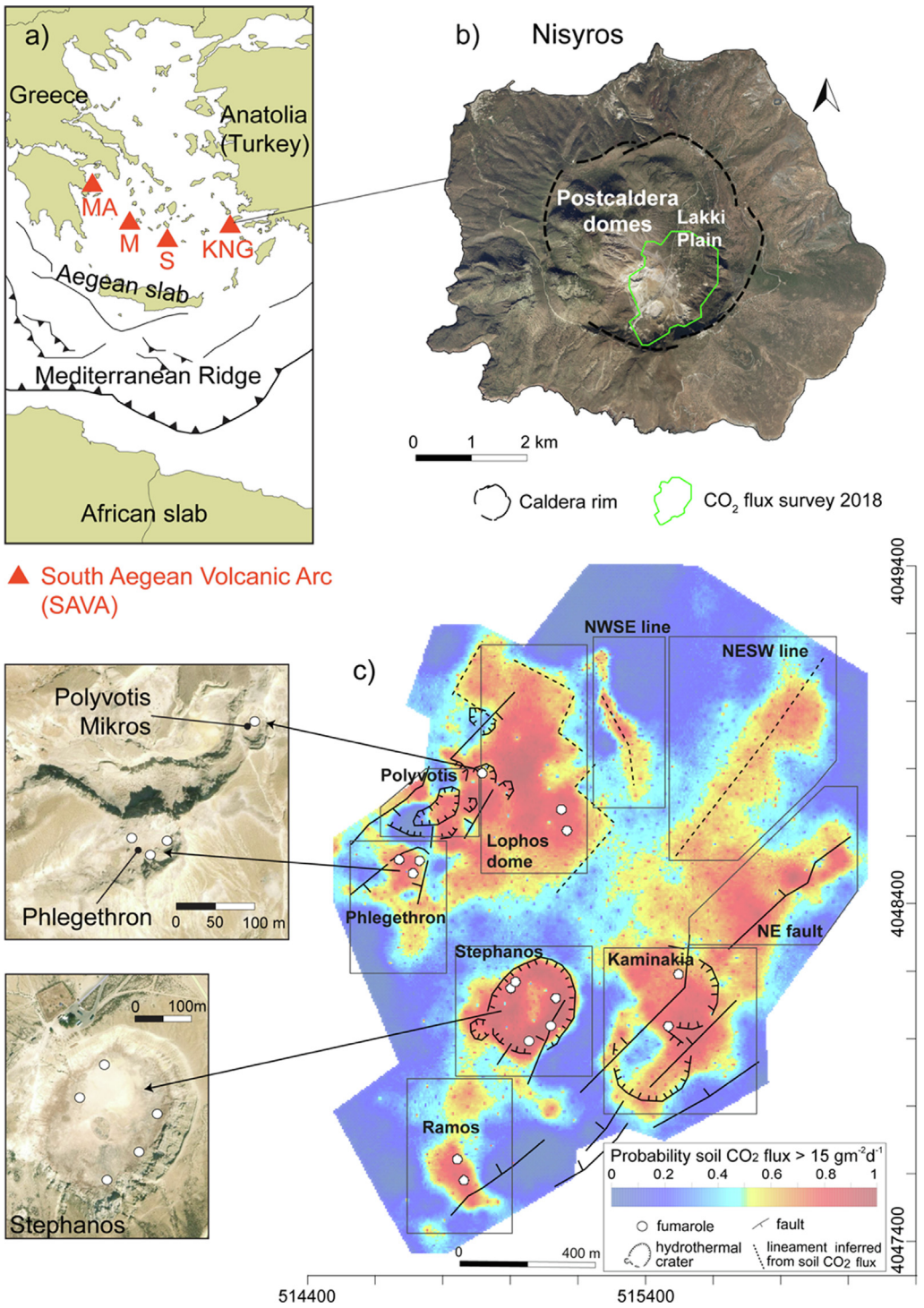

Fig. 1. The South Aegean Volcanic Arc (SAVA; 1a), the Nisyros caldera (1b), and the upflow zone of magmatic-hydrothermal fluids traced by soil CO_2 emission (1c). The SAVA (1a) comprises Kos-Nisyros-Gyali (KNG), Santorini (S), Milos (M), and Methana-Aegina (MA), which result from the northward subduction of the African plate below the Aegean microplate. A minor part of the sediment on the subducted oceanic crust (Eastern Mediterranean Sea) is accreted in the Mediterranean ridge. The Nisyros caldera (1b) is located in the easternmost part of the SAVA and shows many magmatic-hydrothermal fluid emissions in the southern part of its collapse edifice. These emissions have been recently mapped through soil CO_2 flux measurements (green perimeter, Bini et al., 2019), and are spatially distributed over faults, hydrothermal craters (Stephanos, Polyvotis Mikros, Phlegethron, and Kaminakia), and domes (red areas; 1c). The locations of the fumaroles collected in this study are also shown as white circles (1c). (For interpretation of the references to colour in this figure legend, the reader is referred to the web version of this article.)

tion up to 75,000 ppm and originates from the mixing of about 75 % arc-magmatic water and 25 % seawater that percolate in the volcanic edifice (Brombach et al., 2003; Marini and Fiebig, 2005). Buoyancy drives fluid upflow and eventually steam separation at temperatures between 195 and 270 °C at 490–765 m depth (Marini and Fiebig, 2005). This upflowing steam is then emitted into the atmosphere from fumarolic vents, which are mostly located at the bottom of Stephanos, Polyvotis Mikros, Phlegethron, and Kaminakia hydrothermal craters, Lophos dome, and Ramos site (Fig. 1c). However, a large amount of steam is not released into the atmosphere but condenses as it approaches the surface. A recent study based on CO_2 flux measurements shows that the area of

hydrothermal fluid flow extends for about 2.2 km^2 (Bini et al., 2019; Fig. 1c). About 2,000 t d^{-1} of steam condenses below the surface of this area, releasing a thermal energy of about 60 MW. The low-soluble CO_2 of the hydrothermal fluids, on the other hand, is released into the atmosphere through diffuse degassing with an output of about 92 t d^{-1} (Bini et al., 2019).

2.2. Recent activity

Several hydrothermal eruptions occurred after enhanced seismic activity in historical times (Marini et al., 1993 and references therein). A volcano-seismic crisis clustered in time and space between 1996 and 1997. In the area of Nisyros, 113 earthquakes of $M \geq 4.1$ were recorded and >50 % occurred at shallow depth ($\leq$10 km); the largest shock with M = 5.3 occurred on August 1997 (Papadopoulos et al., 1998). A sequence of ground inflation and deflation was also registered during 1995–2000. GPS and SAR interferometry documented ground uplift from 1995 to mid-1998, with a maximum vertical displacement of 140 mm. Then, a gradual subsidence of 70 mm was recorded by GPS in 1999–2000 (Sykioti et al., 2003; Lagios et al., 2005). This ground deformation was modeled with two Mogi point sources related to magma chambers and assuming motion along the Mandraki fault, which was reactivated in 1996 (Lagios et al., 2005). The first chamber was located in the northwestern part of the Nisyros caldera at 5.5 km depth, and the second one 5 km offshore to the north of Nisyros at 6.5 km depth. However, further geodetic, seismic, and geochemical studies (Chiodini et al., 2002; Caliro et al., 2005; Hautmann and Gottsmann, 2018) underlined the important role that the hydrothermal system played on the unrest. For example, earthquakes caused by fluid migration (Long Periods events) were detected at Nisyros from a source located at 1–2 km depth below Lophos dome in 2001, that is the depth of the hydrothermal system (Caliro et al., 2005). Gottsmann et al. (2007) registered short-term (tens of minutes to hours) variation in gravity and deformation with amplitudes up to 25 μGal and 40 mm, respectively. These signals were linked to the instability of the hydrothermal fluid flow regimes, likely due to transient pressure built-up in the hydrothermal system (Caliro et al., 2005; Hautmann and Gottsmann, 2018). The ground upflit of 1995–1998 was then interpreted as a poroelastic response of the host rock due to pore pressure increase of the hydrothermal system during magma degassing (Hautmann and Gottsmann, 2018). The subsequent subsidence was induced by pressure decrease in the hydrothermal system due to fracture opening and fluid transfer to the atmosphere. Chiodini et al. (2002) reported an increase in the proportion of magmatic fluid in the fumaroles after the seismic crisis. The observed increase in CO_2/CH_4 and H_2S/CH_4 ratios in the fumarolic gases was interpreted by these authors as the result of an injection of more oxidizing sulfur-rich magmatic fluids in the hydrothermal system. Shimizu et al. (2005) also reported an increase in the $^3He/^4He$ ratios. During 2001–2002, a 1–5 m wide and up to 10 m deep rupture opened in the central part of the Lakki plain. This phenomenon was caused either by a local accumulation of uncompensated near-surface stresses (Lagios et al., 2005) or by a hydrothermal alteration of the ground from acidic fluid circulation, inducing a collapse (Venturi et al., 2018).

3. Materials and Methods

3.1. Fumarole sampling and analysis

We collected three gas samples from each fumarolic vent located at Polyvotis Mikros, Phlegethron, Stephanos, and Kaminakia hydrothermal craters, Lophos dome, and Ramos site (Fig. 1c) between 2018 and 2021. To sample the gas emission, we inserted a 1 m long stainless-steel tube into the soil, connected to a Pyrex glass pipe. The first sample was collected in a 140 mL evacuated Pyrex glass flask containing 50 mL of a 4 N NaOH solution (Giggenbach, 1975; Giggenbach and Goguel, 1989) connected to the sampling line with silicon tubing. Reactive gases (water vapor, CO_2, and H_2S) are adsorbed in the alkaline solution, whereas non-reactive gas species (N_2, O_2, CO, H_2, He, Ar, and CH_4) occupy the flask headspace. The second and third samples were collected simultaneously after connecting a water-cooled condenser to the sampling line. The gas emission circulates in the condenser leading to vapor phase condensation, while the remaining dry gas phase is collected into a 20 mL Pyrex glass flask equipped with two Teflon stopcocks. The second sample consists of this dry gas phase, and the third sample is the corresponding steam condensate stored in a 50 mL high-density polyethylene bottle. Precautions were adopted to minimize any air contamination during the entire sampling procedure, such as a submerged exhaust after the glass flask, sealing of the sampling line junctions through gaskets and/or a high-vacuum grease, and a slow gas pumping (second and third samples) to avoid depressurization into the line.

The three samples collected for each vent were then specifically analyzed at the Laboratory of the *Istituto Nazionale di Geofisica e Vulcanologia, Sezione di Napoli, Osservatorio Vesuviano* (INGV-OV), to determine the chemical and isotopic composition of the fluids. The instrumentation and protocols adopted are described in detail in Caliro et al. (2015). The first sample was used for the determination of He, H_2, Ar, O_2, N_2, and CH_4 contents and nitrogen and argon isotopes in the flask headspace by continuous flow mass spectrometry (Thermo Finningan Delta plus XP) coupled with gas chromatography (Agilent Technologies 6890 N). Importantly, these chemical and isotopic analyses were carried out on the same aliquot of sample through a single gas injection into the instrumental apparatus. The gas is injected into the gas chromatograph, which is composed by two channels equipped with two six-port injection valves, two PLOT columns (MolSiev, 5 Å; 30 m × 0.53 mm × 50 μm; He and Ar as carrier gases), and thermal conductivity detectors. The first channel serves for He and H_2 analysis using Ar as carrier gas. The second channel was equipped with a post-column switching device that enable the column gas flow (sustained by He as carrier gas) to be split both to the thermal conductivity detector for Ar, O_2, N_2, and CH_4 analyses, and to the mass spectrometer through an open split. The mass spectrometer was equipped with a universal triple collector to simultaneously determine ^{36}Ar and N isotopes. The alkaline solution in the first sample was then oxidized by H_2O_2 to completely transform the absorbed H_2S into SO_4^{2-} and analyze it by ion chromatography (Dionex ICS-3000). The CO_2 contents were determined by analyzing CO_3^{2-} by acidimetric titration (analytical error ±3 %). The second sample (dry gas phase) was analyzed for CO contents by gas chromatography, thus avoiding possible reactions in alkaline solution to form $COOH^-$ (Giggenbach and Matsuo, 1991). The concentration of CO, expressed in ppm in volume, was then used to compute the complete gas composition considering only the dry gas species (i.e., without water). In the second sample, further analyses of carbon and oxygen isotopes of CO_2 were also performed by mass spectrometry after gas chromatographic separation using the GasBench II device. The third sample (steam condensate) was used to analyze the hydrogen and oxygen isotopes of H_2O with a near infrared laser analyzer (Picarro L2130-i).

To measure the helium isotope contents in the gas emission, a double NaOH sample was collected for Polyvotis Mikros, Phlegethron, Stephanos, and Lophos vents. These samples were analyzed at the Laboratory of the *Istituto Nazionale di Geofisica e Vulcanologia, Sezione di Palermo* (INGV-PA). The isotopic composition of He ($^3He/^4He$) and ^{20}Ne in the flask headspace was analyzed using

the method and analytical procedure described in Rizzo et al. (2016), and corrected for atmospheric contamination using the ^{4}-He/^{20}Ne ratio (Sano and Wakita, 1985).

3.2. Binary mixing modeling

Mixing models are useful tools to estimate the contents of two or more components (or endmembers) that mutually contribute to the whole chemical composition of gas, liquid, and solid samples. Based on mass-balance equations, Vollmer (1976) and Langmuir et al. (1978) demonstrated that binary mixtures of ratios of elements or isotopes plotted in the x–y space distribute along a rectangular hyperbola. If the compositions of the two endmembers are known, a forward modeling can predict the composition of the binary mixtures along the mixing hyperbola. Contrarily, if the endmembers compositions are unknown, they can be estimated by using a reverse modeling based on the method of least squares (Albarède, 1995; Janoušek et al., 2016).

3.2.1. Definition of the endmembers by reverse mixing modeling

3.2.1.1. Mixing hyperbola. The endmembers at the extremities of the hyperbolic curve can be estimated by linear regression following Albarède (1995) and Janoušek et al. (2016). The equation of the binary mixing hyperbola can be written as

$$xy = x_0 y + y_0 x + q - x_0 y_0 \quad (1)$$

where x and y are the ratios of elements or isotopes, x_0 and y_0 are the vertical and horizontal asymptotes, respectively, and q is the curvature factor of the hyperbola. This equation reflects the general formula of a multiple linear regression model, which for the ith observation takes the form

$$Y_i = \beta_0 + \beta_1 x_{i1} + \beta_2 x_{i2} + \varepsilon_i \quad (2)$$

where Y is the response variable, $\beta_0 = q - x_0 y_0$, $\beta_1 = x_0$, and $\beta_2 = y_0$ are the regression coefficients, $x_1 = y$, and $x_2 = x$ are the predictors, and ε is the random error. The three regression coefficients β_0, β_1, and β_2, and therefore the three coefficients of the hyperbola x_0, y_0, and q, are estimated using the method of least squares (see supplementary material) with the built-in R (R Core Team, 2022) function *lm*. After rearranging Eq. (1) to

$$y = y_0 + \frac{q}{(x - x_0)} \quad (3)$$

the three coefficients estimated are used to plot the mixing hyperbola in the x-y space. Since the compositions of the endmembers exist between the data at the extremities of the hyperbola and infinite, that is where the curvature becomes almost straight, its actual definition is not trivial. Therefore, the asymptotes values (x_0 and y_0) are reasonably selected as an estimate of the endmember compositions (e.g., Labanieh et al., 2010). An R script for calculating the composition of unknown endmembers through the mixing hyperbola method is provided as Supplementary Material.

3.2.1.2. Mixing straight line. Binary mixtures of ratios with the same denominator plot along a straight line that connects the two endmembers. Mixing lines are therefore obtained by performing simple linear regression on the data through the built-in R (R Core Team, 2022) function *lm*, which consists in finding two regression coefficients β_0 and β_1 by the method of least squares. Then, the endmember composition is extrapolated from the regression line through the built-in R function *predict*.

3.2.1.3. Checking of linear model assumptions. To reasonably fit either a multiple or a simple linear model by least squares, as in the mixing hyperbola and straight-line cases, some assumptions need to be fulfilled. In particular, we need to consider that (i) the variance of the errors (ε) is constant, (ii) the errors are uncorrelated and (iii) normally distributed. To this end, we inspected both the Tukey-Anscombe plot and the QQ (quantile–quantile) plot (Figs. S1, S2, S3) of the residuals, which are estimates of the errors ε. The Tukey-Anscombe plot (Figs. S1a, S2a, and S3a) shows the residuals plotted against the fitted values and is used for checking assumptions (i) and (ii). In the ideal case of constant variance of the errors, the points are randomly distributed around the horizontal line through zero. The QQ plot (Figs. S1b, S2b, and S3b) shows the empirical quantiles of the residuals versus the theoretical quantiles of a normal distribution with mean equal to 0 and standard deviation equal to 1. In the ideal case of a normal distribution of the errors, that is the assumption (iii), the points distribute along the grey dashed line. Both plots allow us to identify outliers that affect the quality and accuracy of the model and therefore of the prediction. In the presence of outliers, the exclusion of these points ensures the fulfillment of these assumptions as well as a reduction of the residual standard error (RSE), that is an estimate of the standard deviation of ε. As a consequence, the error associated with each prediction also decreases.

3.3. Gas geoindicators of the T of the hydrothermal system

The composition of reactive species in fumarolic gases is used to estimate the temperature of the hydrothermal system using the method of Chiodini and Marini (1998). This method assumes that (i) the H_2O-H_2-CO_2-CH_4-CO gas system is in chemical equilibrium, (ii) the fumaroles are representative of the vapor phase separated through boiling at temperature *Ts* from an original liquid at temperature *To*, and (iii) the boiling is an adiabatic process. Theoretical compositions of the vapor phase separated at *Ts* are calculated by the following mass and enthalpy balances

$$\left(\frac{X_i}{X_{H_2O}}\right)_{l,To} = (1-s)\left(\frac{X_i}{X_{H_2O}}\right)_{l,Ts} + s\left(\frac{X_i}{X_{H_2O}}\right)_{v,Ts} \quad (4)$$

$$h_{l,To} = (1-s)h_{l,Ts} + s h_{v,Ts} \quad (5)$$

where X_i is the mole fraction of the ith species, subscripts l ad v refer to liquid and vapor phases, respectively, s is the fraction of vapor separated through boiling, and h is the specific enthalpy (kJ kg^{-1}). These compositions are then plotted in the $3\log(X_{CO}/X_{CO2})$ + $\log(X_{CO}/X_{CH4})$ vs $\log(X_{H2O}/X_{H2})$ + $\log(X_{CO}/X_{CO2})$ diagram (Fig. S4). The original temperature *To*, the separation temperature *Ts*, and the fraction of the separated vapor *s* are estimated by comparing the analytical values with the theoretical compositions in Fig. S4. The energy released from the hydrothermal system per kg of vapor separated through boiling is expressed as $s\ h_{v,Ts}$ in Eq. (5), where $h_{v,Ts}$ is the specific enthalpy of the vapor phase at temperature *Ts*. We suggest to read the work of Chiodini and Marini (1998) for an exhaustive explanation of the methodology.

4. Results

4.1. Gas composition

Temperatures and chemical and isotopic compositions of gases collected between 2018 and 2021 within the Nisyros caldera (Fig. 1c) are reported in Table 1. Measured temperatures (*T* in °C) of the vent emissions are close to water boiling *T*, that is 99.6 °C at ~120 m above sea level, ranging between 94.8 and 107.0 °C. The lowest *T* were registered at Kaminakia vents, which experienced the greatest subsurface steam condensation according to studies on water stable isotopes (Brombach et al., 2003; Marini and Fiebig, 2005). The highest *T* were measured at Polyvotys Mikros vent. Water is by far the most abundant component in the

Table 1
Chemical and isotopic compositions of the fumarolic fluids collected at Nisyros between 2018 and 2021. The chemical composition is reported in μmol/mol. Isotopic compositions of O and H, C, and N are reported in delta notation (‰) relative to V-SMOW, V-PDB, and atmosphere, respectively. He isotope ratio is divided by the ratio in air (Ra) and corrected for atmospheric contamination based on the $^4He/^{20}Ne$ ratio (Sano and Wakita, 1985).

Sample	Location	Date	*T* (°C)	H_2O	CO_2	H_2S	Ar	O_2	N_2	CH_4	H_2	He	CO	$\delta^{18}O_{H2O}$	δD_{H2O}	$\delta^{13}C_{CO2}$	$\delta^{18}O_{CO2}$	$\delta^{15}N$	$^{40}Ar/^{36}Ar$	$^3He/^4He$	$^4He/^{20}Ne$
POLIBOTEMICRò	Polyvotis Mikros	2018–10–04	100.8	986,209	11,215	2355	0.10	0.017	15.5	39.8	165.5	0.34	0.067	3.41	−8.8	−0.24	35.27	4.31	374.8	n.d.	n.d.
POLIBOTEMICRò II	Polyvotis Mikros	2018–10–04	100.8	986,594	10,799	2417	0.09	0.015	13.2	32.5	143.4	0.28	0.065	3.41	−8.8	−0.24	35.27	4.13	348.8	n.d.	n.d.
STE 1	Stephanos	2018–10–11	101.8	982,616	14,036	3012	0.23	0.012	29.2	180.6	125.7	0.39	0.027	4.58	−7.5	−1.50	35.63	2.23	327.5	n.d.	n.d.
STE 2	Stephanos	2018–10–11	100.6	983,474	12,971	3307	0.28	0.014	31.4	90.0	125.3	0.39	0.024	4.41	−6.0	−0.92	36.11	−1.55	315.5	n.d.	n.d.
FLEG. Alex	Phlegethron	2018–10–04	100.1	982,433	13,898	3485	0.23	0.019	26.6	23.1	133.5	0.43	0.025	2.21	−0.3	−0.39	32.81	4.43	327.4	n.d.	n.d.
KAMINAKIA	Kaminakia	2018–10–04	99.7	916,918	74,203	6169	2.04	0.190	199.6	1628.7	877.5	1.21	0.223	−7.11	−45.9	−0.91	30.94	0.62	305.5	n.d.	n.d.
LOFOS	Lophos dome	2018–10–11	99.0	981,405	14,817	3444	0.77	0.023	76.7	123.6	132.3	0.50	0.073	−0.06	−22.4	−0.96	30.91	−9.74	295.0	n.d.	n.d.
LOFOS	Lophos dome	2018–10–03	100.3	975,742	18,734	4050	13.99	0.000	1141.9	148.6	169.6	0.67	0.095	−0.06	−22.4	−0.96	30.91	−1.55	299.0	n.d.	n.d.
RAMOS	Ramos	2018–10–03	96.0	966,806	29,056	2241	6.55	0.000	566.2	676.2	647.8	0.68	0.192	−9.61	−68.6	−1.62	24.07	−19.15	298.0	n.d.	n.d.
POLIBOTEMICRO	Polyvotis Mikros	2019–04–04	99.7	987,068	10,794	1919	0.25	0.009	25.6	34.8	157.7	0.31	0.071	1.69	−16.4	−0.35	38.02	3.02	327.0	n.d.	n.d.
POLIBOTEMICRO SUD	Polyvotis Mikros	2019–04–11	99.7	984,406	13,101	2248	0.10	0.007	16.9	48.0	179.2	0.39	0.125	−2.93	−38.1	−0.07	31.84	7.02	420.4	n.d.	n.d.
STE 1	Stephanos	2019–04–05	99.1	984,898	12,560	2286	0.17	0.017	21.2	126.5	108.2	0.32	0.073	2.72	−15.5	−0.98	37.02	5.26	351.5	n.d.	n.d.
STE 2	Stephanos	2019–04–05	99.3	983,640	13,489	2872	n.d.	n.d.	n.d.	n.d.	n.d.	n.d.	0.083	0.96	−23.0	−0.80	36.66	5.94	n.d.	n.d.	n.d.
PHLEGETON	Phlegethron	2019–04–04	99.7	982,716	14,206	2895	0.19	0.045	22.4	22.8	136.3	0.44	0.040	−0.13	−13.4	−0.33	34.67	5.01	348.6	n.d.	n.d.
PHLEGETON 2 NORD	Phlegethron	2019–04–11	99.8	980,221	16,123	3469	0.17	0.000	22.8	24.8	138.9	0.43	0.072	−6.45	−42.5	−0.57	29.76	5.88	338.4	n.d.	n.d.
KAMINAKIA	Kaminakia	2019–04–04	97.4	920,860	66,675	4340	78.38	0.000	5810.6	1411.3	831.3	1.37	0.344	−10.18	−62.6	−0.81	26.39	0.22	295.5	n.d.	n.d.
LOFOS	Lophos dome	2019–04–04	99.4	983,679	13,301	2789	0.21	0.019	22.0	95.9	112.0	0.39	0.060	−5.30	−49.6	−0.85	29.96	4.57	328.9	n.d.	n.d.
RAMOS	Ramos	2019–04–04	n.d.	970,609	25,651	1759	11.54	0.000	939.6	593.1	436.8	0.63	0.113	−5.25	−39.3	−1.49	30.00	−10.27	295.4	n.d.	n.d.
PMN II	Polyvotis Mikros	2019–10–14	107.0	984,652	12,973	2152	0.08	0.007	15.0	45.9	161.3	0.35	0.063	2.15	−14.8	−0.14	36.35	6.76	394.3	6.03	5286
PMS II	Polyvotis Mikros	2019–10–14	102.0	985,803	11,854	2119	0.08	0.007	14.7	44.8	163.8	0.37	n.d.	1.81	−17.6	−0.10	35.89	6.79	394.5	5.96	4470
STEF 1	Stephanos	2019–10–15	99.3	983,576	13,352	2652	2.12	0.000	175.3	128.7	113.4	0.40	0.042	3.79	−10.3	−1.10	37.94	0.38	299.7	5.94	3984
STEF 3 II	Stephanos	2019–10–15	99.2	983,543	13,591	2576	0.17	0.010	23.0	147.8	118.9	0.38	n.d.	2.62	−16.3	−1.04	37.39	5.44	349.6	5.70	4310
PHLEGETON 1	Phlegethron	2019–10–14	100.5	983,954	13,039	2845	0.14	0.023	19.2	20.1	121.9	0.37	n.d.	0.49	−10.3	−0.57	35.90	5.62	347.2	6.22	4231
PHLEGETON 2	Phlegethron	2019–10–14	100.0	983,676	13,285	2867	0.16	0.019	21.1	21.9	127.9	0.41	0.047	1.76	−2.3	−0.61	36.19	5.60	350.7	5.51	2098
KAMINAKIA	Kaminakia	2019–10–13	94.8	905,741	81,728	5563	51.06	0.000	4113.6	1785.1	1017.5	1.54	n.d.	−10.11	−62.8	−0.87	26.70	−1.63	298.6	n.d.	n.d.
LOFOS II	Lophos dome	2019–10–13	99.8	983,494	13,406	2838	0.67	0.017	62.0	96.0	103.6	0.39	n.d.	−1.13	−27.8	−1.10	33.25	1.24	307.7	5.99	128
RAMOS	Ramos	2019–10–15	n.d.	882,741	99,718	7878	59.23	0.000	4819.8	3014.2	1767.7	2.94	0.372	−6.03	−45.5	−1.69	29.02	−0.41	299.0	n.d.	n.d.
PMN5	Polyvotis Mikros	2021–10–09	99.2	988,075	10,196	1583	0.04	3.002	9.1	27.3	106.5	0.22	0.048	1.00	−21.0	−0.83	35.60	7.05	336.6	5.93	7177
S1	Stephanos	2021–10–08	99.3	n.d.	n.d.	n.d.	n.d.	n.d.	n.d.	n.d.	n.d.	n.d.	n.d.	2.88	−13.9	−2.34	38.36	n.d.	n.d.	n.d.	n.d.
S2	Stephanos	2021–10–08	100.6	985,247	12,430	2045	0.16	4.207	21.1	145.9	106.1	0.31	0.034	3.96	−8.8	−2.57	38.87	2.57	332.6	5.80	2733
S3	Stephanos	2021–10–08	99.6	970,370	23,299	4160	21.76	4.552	1670.0	234.9	236.9	2.08	0.065	2.60	−15.5	−2.62	38.52	0.03	306.7	n.d.	n.d.
PH6	Phlegethron	2021–10–10	99.5	985,460	12,282	2103	0.17	0.016	21.3	25.4	107.4	0.33	0.050	1.01	−8.1	−1.07	35.12	4.84	321.1	5.81	2237

fumaroles, followed by high concentrations of CO_2 (10,196–99,71 8 ppm) and H_2S (1,583–7,878 ppm). Nitrogen contents extend from 13 to 5,811 ppm, with the highest values measured in Kaminakia and Ramos fumaroles. These samples also show the highest CH_4 and H_2 contents, ranging from 593 to 1,785 ppm, and 437 to 1,018 ppm, respectively. Argon, He, and CO vary between 0.04 and 78.12 ppm, 0.22 and 2.94 ppm, and 0.02 and 0.37 ppm, respectively. Acidic gases (SO_2, HCl, HF) are not present in Nisyros fluids, whereas significant amounts of reduced gas species (H_2S and CH_4) were measured. This evidence reflects a hydrothermal origin of the Nisyros fumaroles, as already reported in previous studies (Chiodini et al., 1993; Brombach et al., 2003; Caliro et al., 2005, Marini and Fiebig, 2005).

Oxygen and hydrogen isotopes of steam condensates reported in delta notation relative to V–SMOW ($\delta^{18}O_{H2O}$ and δD_{H2O}, respectively) show a wide range from –10.18 to 4.58 ‰, and from –68.64 to –0.29 ‰, respectively (see δD_{H2O} versus $\delta^{18}O_{H2O}$ diagram, Fig. S5), consistently with the data reported from previous studies (Brombach et al., 2003; Marini and Fiebig, 2005). According to these studies, these large variations in $\delta^{18}O_{H2O}$ and δD_{H2O} are caused by steam condensation at water-boiling temperature, thus forming ^{18}O–and–^{2}H–depleted residual vapors (dashed lines in Fig. S5). This process is particularly evident in Kaminakia fumaroles (Fig. S5). The heaviest isotopes recorded in Polyvotis Mikros and Stephanos gases approach the composition of the deep magmatic-hydrothermal liquid (also called Parent Hydrothermal Liquid, PHL, by Marini and Fiebig, 2005) on the seawater arc-type-magmatic water mixing line (Brombach et al., 2003; Marini and Fiebig, 2005). According to these authors, these vapors separate from the PHL, which is an admixture of ~75 % arc-magmatic water and 25 % seawater. Carbon isotopes of CO_2, reported in delta notation relative to PDB ($\delta^{13}C_{CO2}$), extend from –2.62 to –0.07 ‰, within the range of the Nisyros magmatic-hydrothermal CO_2 defined by Bini et al. (2020).

Nitrogen isotope values ($\delta^{15}N$) determined for the Nisyros fumaroles range from –19.1 to 7.0 ‰ relative to air (i.e., 0 ‰). The very ^{15}N-depleted samples (two from Ramos, October 2018 and April 2019, and one from Lophos, October 2018; –19.2, –10.3, and –9.7 ‰, respectively) were collected from fumaroles with low and variable fluxes and are among those most contaminated by air, as shown by the $^{40}Ar/^{36}Ar$ ratios (295.0–298). Therefore, we excluded these gases because they appear affected by some N mass-dependent fractionation processes (e.g., mass-dependent fractionation of air; Labidi et al., 2020). Excluding these samples, $\delta^{15}N$ span the range between –1.6 and 7.0 ‰, with the most positive values measured at Polyvotis Mikros, Phlegethron, and Stephanos. Notably, these latter fumaroles also show the highest $^{40}Ar/^{36}Ar$ ratios (up to 420.4). Measured helium isotope ratios ($^{3}He/^{4}He$) reported relative to the atmospheric ratio (Ra = 1.39×10^{-6}) range between 5.51 and 6.22 Ra and are characterized by high $^{4}He/^{20}Ne$ ratios (up to 7,177), suggesting a relatively low air contamination for He and Ne.

4.2. Binary mixing modeling of N_2, He, and Ar reveals the current composition of a deep magmatic endmember

The relative concentrations of N_2, He, and Ar in the fumaroles are visualized in the ternary diagram of Fig. 2. These gases show an evident mixing trend between a deep endmember located towards the He apex and air, with negligible contributions from air-saturated water (ASW). It is worth noting that the deep magmatic endmember plots in the typical upper mantle region of the diagram, showing very low N_2/He and N_2/Ar ratios with respect to those of typical gases from arc volcanoes (grey band in Fig. 2).

N_2, He, and Ar gas ratios of the deep endmember are estimated with reverse binary mixing modeling using both the hyperbola and straight-line models (Sections 3.2.1.1 and 3.2.1.2; Figs. 3, 4). Results are shown in the next subsections and summarized in Table 2. To fit these linear models, we excluded a few outliers that affect their quality (Section 3.2.1.3). The exclusion of these points enables the fulfillment of the assumptions for all the models (see Section 3.2.1.3; Figs. S1, S2, S3) as well as substantial error reduction in predicting the deep endmember. Notably, these outliers correspond either to fumaroles collected after some heavy rainy days in April 2019, which were influenced by shallow ASW contamination and secondary processes, or vents sampled in 2021, when lower gas fluxes were observed. Most selected data (19 samples out of 22) were collected during the dry season in October 2018, 2019, and 2021.

4.2.1. The $N_2/^4He_{deep}$ ratio

Nisyros fumaroles show a hyperbolic relationship in the $N_2/^4He$-$^{40}Ar/^{36}Ar$ space, which reflects a binary mixing between air and a deep source (Fig. 3). We applied the mixing hyperbola method (Section 3.2.1.1) to this space to estimate the $N_2/^4He$ ratio of the deep endmember ($N_2/^4He_{deep}$). The best fit of the data solved by the method of least squares (see Section 3.2.1.1), the variability of the fitted coefficients, and the goodness-of-fit are summarized in Table 3. Notably, the vertical asymptote of the hyperbola x_0 (dashed line) closely approaches the $^{40}Ar/^{36}Ar$ ratio measured in air (298.6; Lee et al., 2006). Therefore, x_0 defines the air endmember (black star). The horizontal asymptote y_0 (dashed line) of the hyperbolic fit defines the $N_2/^4He_{deep}$ ($y_0 = N_2/^4He_{deep}$) ratio, which is equal to 31.8 ± 4.5 (95 % confidence interval; light green band).

4.2.2. The $^{36}Ar/^4He_{deep}$ ratio

Plotting one of the ratios of the binary mixing hyperbola (Fig. 3), such as $N_2/^4He$, versus that of $^{36}Ar/^4He$ (i.e., the ratio of denominators Fig. 4a), enables us to check the air-deep binary mixing (Langmuir et al., 1978) and estimate the $^{36}Ar/^4He$ ratio of the deep endmember ($^{36}Ar/^4He_{deep}$). Nisyros fumaroles show a linear relationship (Fig. 4a), extending from a low-$N_2/^4He$-$^{36}Ar/^4He$-deep endmember towards the air composition (inset in Fig. 4a), therefore confirming the binary mixing. To estimate the $^{36}Ar/^4He_{deep}$ ratio, we used the mixing straight line method (Section 3.2.1.2). The fitted coefficients of the linear regression model, their variability, and the goodness of fit are summarized in Table 4. The $^{36}Ar/^4He_{deep}$ ratio can be estimated by using $N_2/^4He_{deep}$ = 31.8 as predictor (Fig. 4b), and the uncertainty of the measure was calculated according to the 68 % (i.e., 1 σ) prediction band of the regression line (light blue band in Fig. 4b). The prediction yields a $^{36}Ar/^4He_{deep} = 2.05 \times 10^{-4} \pm 1.88 \times 10^{-4}$. We chose the 68 % prediction band to avoid negative values in the lower limit of the estimate, which result by choosing a prediction interval >68 %.

4.2.3. The $N_2/^{36}Ar_{deep}$ and $^{40}Ar/^{36}Ar_{deep}$ ratios

In a similar way, fumaroles are linearly correlated in the $N_2/^{36}Ar$–$^{40}Ar/^{36}Ar$ space, and the linear regression model precisely intercepts the air composition and extends toward an unknown high-$N_2/^{36}Ar$–$^{40}Ar/^{36}Ar$-deep endmember (Fig. 4c). In this plot, we applied the mixing straight line method (Section 3.2.1.2) to estimate the $^{40}Ar/^{36}Ar$ ratio of the deep endmember ($^{40}Ar/^{36}Ar_{deep}$). A summary of the fitted coefficients and the goodness of fit is shown in Table 5. First, we calculated the $N_2/^{36}Ar$ ratio of the deep endmember ($N_2/^{36}Ar_{deep}$), which is equal to 155,353, by dividing $N_2/^4He_{deep}$ (31.8) by $^{36}Ar/^4He_{deep}$ (2.05×10^{-4}). Then, we used this value to extrapolate the $^{40}Ar/^{36}Ar_{deep}$ ratio from the 95 % prediction band of the regression line (light blue band in Fig. 4c), yielding an estimate of 551.6 ± 19.8. Considering the uncertainty of the $N_2/^4He_{deep}$ (31.8 ± 4.5; 95 % CI), the usage of its lower limit (27.3) for extrapolation would return $N_2/^{36}Ar = 1.64 \times 10^6$ and $^{40}Ar/^{36}Ar$ = 3,417 ± 239 (between brackets in Table 2), which reflect

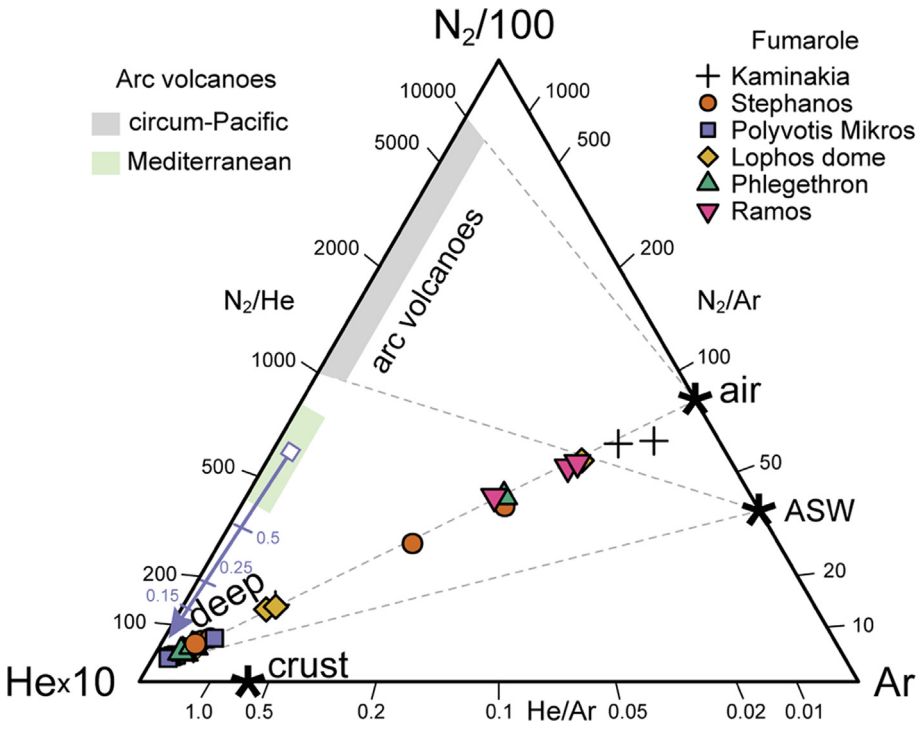

Fig. 2. Relative contents of N_2, He, and Ar in Nisyros fumaroles. ASW, air, crust, and a deep magmatic endmember are shown for comparison. The crust endmember was defined by Giggenbach (1996) for New Zealand gases. The typical composition of arc volcano gases (grey band), defined by most circum-Pacific systems, and the composition of the Mediterranean arc gases (light green band), defined by Vulcano, Campi Flegrei, and Milos (Giggenbach, 1991, 1996, 1997), are also displayed. The $N_2/^4He$ ratios of the Mediterranean arc field defined by Giggenbach (1997) (light green band), that is 400–800, also include the magmatic gas components defined at Vulcano by Taran (2011) and Paonita et al. (2013), and at Campi Flegrei by Caliro et al. (2014). Nisyros fumaroles are binary admixtures of air and a deep endmember. The purple arrow reflects the degassing trend and the remaining gas fraction in an evolved arc magma with an initial N_2/He = 600 (the average of Mediterranean arc-gas; see Section 5.1). (For interpretation of the references to colour in this figure legend, the reader is referred to the web version of this article.)

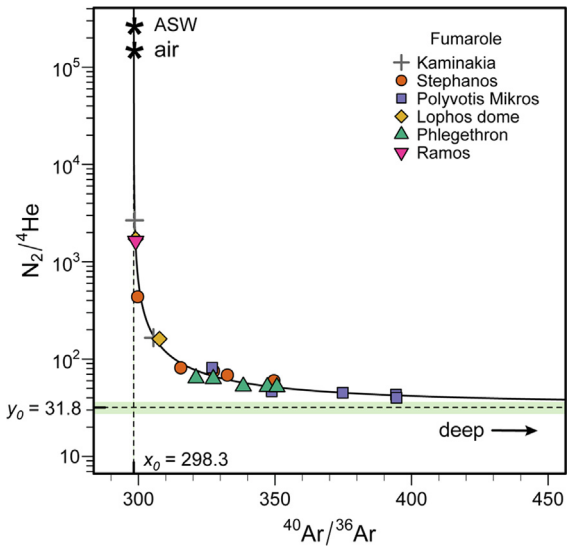

Fig. 3. $N_2/^4He$ as a function of Ar isotopes. The hyperbolic relationship of Nisyros fumaroles reveals a binary mixing between air and a deep endmember. The air endmember is estimated by the vertical asymptote x_0 of the best hyperbolic fit (hyperbola), while its horizontal asymptote y_0 defines the $N_2/^4He$ ratio of the deep endmember ($N_2/^4He_{deep}$). The light green band represents the 95% confidence interval of $N_2/^4He_{deep}$. The composition of air saturated water (ASW) is also shown for comparison. (For interpretation of the references to colour in this figure legend, the reader is referred to the web version of this article.)

the maximum values expected from the models. However, it is worth noting that this high degree of uncertainty entirely hinges on the choice of a large confidence interval (95 %) for $N_2/^4He_{deep}$.

4.2.4. The $\delta\ ^{15}N_{deep}$

Nitrogen isotope data plotted against $N_2/^3He$, $N_2/^4He$, and $N_2/^{36}Ar$ ratios predominantly show a mixing trend between air and a deep endmember (light blue band, Fig. 5). Using the $N_2/^{36}Ar_{deep}$, $N_2/^4He_{deep}$, and $N_2/^3He_{deep}$ ratios (Table 2) in the mixing equations of Sano et al. (2001) and Fischer et al. (2002), we computed nitrogen isotopes of the deep endmember ($\delta\ ^{15}N_{deep}$) equal to 7 ± 3 ‰. This value overlaps the range of the subducted sedimentary nitrogen (i.e., 7 ± 4 ‰) defined by Sano et al. (2001), including both the organic N in marine sediments ($\delta\ ^{15}N$ between 2 and 10 ‰; Peters et al., 1978) and the NH_4^+ in metasediments ($\delta\ ^{15}N$ between 2 and 15 ‰; Bebout and Fogel, 1992). The most positive $\delta\ ^{15}N$ values of metasediments reflect the residual subducted N (fixed as NH_4^+ in phyllosilicate) after devolatilization at high metamorphic grade (Bebout and Fogel, 1992). Upper mantle, often called depleted mid-ocean ridge basalt (MORB) mantle (DMM), and sedimentary endmembers (Table 2) are also shown for comparison.

4.3. Temporal variation in reactive and nonreactive (N_2, He, and Ar) gases between 1990 and 2021

The time series of the CO_2/CH_4, He/CH_4, and He/CO_2 ratios measured in the fumaroles of Polyvotis Mikros, Stephanos, and Phlegethron from 1990 to 2021 are reported in Fig. 6a. The dataset includes 2018–2021 data (this study) and those of Chiodini et al. (2002) and Chiodini (2009), along with results analyzed at the Department of Earth Sciences of the University of Florence (Italy) using similar techniques (see Vaselli et al., 2006; Supplementary Material). All fumarolic vents show an increase in both CO_2 and He relative to CH_4 after the 1996–1997 seismic crisis, with the

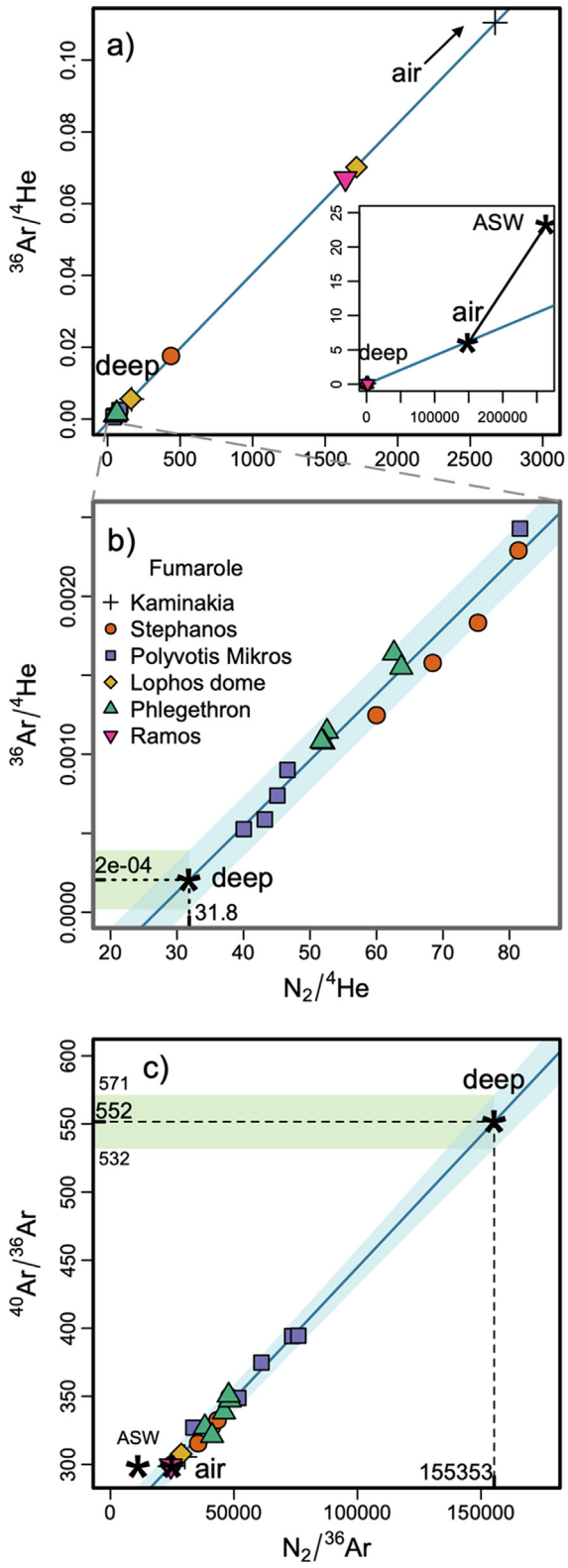

Fig. 4. $^{36}Ar/^{4}He$ as a function of $N_2/^{4}He$ (4a, b) and $^{40}Ar/^{36}Ar$ as a function of $N_2/^{36}Ar$ (4c). Nisyros fumaroles show a linear relationship between air and a deep endmember. The coefficients of the linear models are shown in Table 4 (4a, b) and Table 5 (4c). The inset in 4a represents a reduction of the diagram, whereas 4b is an enlargement. Light blue bands are 68 % and 95 % prediction interval for 4b and 4c, respectively. The $^{36}Ar/^{4}He_{deep}$ and $^{40}Ar/^{36}Ar_{deep}$ ratios are extrapolated from these linear regression models using $N_2/^{4}He_{deep}$ = 31.8 and $N_2/^{36}Ar_{deep} = 1.55 \times 10^5$, respectively. Light green bands represent the errors associated to the prediction. (For interpretation of the references to colour in this figure legend, the reader is referred to the web version of this article.)

highest ratios recorded in 2001–2002. Subsequently, the CO_2/CH_4 and He/CH_4 ratios decrease down to background values and show an almost stationary trend until 2021. A similar trend is also observed in the He/CO_2 time series. The equilibrium temperature of the hydrothermal system (*To*; see Section 3.3) also increases after the seismic crisis (Fig. 6b). This variation is particularly clear in the fumaroles of Polyvotis Mikros and correlates with an increment in the fraction of vapor (s) that separates from the boiling hydrothermal liquids and the correspondent energy released ($s \times h_{v,Ts}$).

We compare N_2, He, and Ar contents in Nisyros fumaroles collected between 2018 and 2021 (this study) with those measured during the peak in 1999–2002 in the Ar/N_2-He/N_2 space (Fig. 7). These gases distribute as ternary admixtures of air, ASW, and deep endmembers. The lower edge of the triangle is defined by the binary air-deep admixture of the 2018–2021 fumaroles (white sample) and the current deep endmember estimated in the previous sections (Table 2). The 95 % prediction band of the linear regression model (light blue band) and the maximum value of the deep endmember (blue star), predicted by using the lower limit of the 95 % CI of the $N_2/^{4}He_{deep}$ ratio (27.3), are also shown. Notably, fumaroles point to an increase in both ASW and deep component during the peak of the CO_2/CH_4 and He/CH_4 ratios (Fig. 6a) in 1999–2002 (grey sample). This increment in the fraction of ASW (f_{ASW}) over time is also shown in Fig. 6c.

5. Discussion

5.1. Origin of the deep endmember in the current fluid emission

N_2, Ar, and He reveal that Nisyros fumaroles are binary admixtures of an atmospheric-like component and a deep endmember. The atmospheric component is almost solely air, not ASW, implying a shallow mixing with atmosphere. This may reflect both the contamination occurring during the sampling of the gas at the surface, and the entrainment of air in the fumarolic channels, which is favored when fumarole fluxes are low (particularly at Kaminakia and Ramos). Part of the air endmember might also be degassed ASW, since for very small fraction of vapor separated (corresponding to a smaller degree of boiling and low fumarole fluxes) the composition of the gas phase may approach that of air. Although the N_2-He-Ar systematics may show some (small) percentages of air in the gases, it is important to note that the degree of air contamination in the total sample composition is negligible. For example, assuming N_2 content as entirely atmospheric (which is an overestimate since part of N derives from the magmatic component), the fraction of air in Polyvotis Mikros gases would be <0.00003. The other term of the binary mixture, that is the deep endmember, reflects a component of magmatic origin dissolved in the hydrothermal fluids. Notably, the fumaroles showing CO_2/CH_4 and He/CH_4 peaks during the unrest (Fig. 6a; Polyvotis Mikros, Phlegethron, and Stephanos) are the most enriched in the deep component (Figs. 2–5). These vents show $^{40}Ar/^{36}Ar$ and $^{3}He/^{4}He$ ratios up to 420 and 6.2 Ra, respectively, and $\delta\ ^{15}N$ up to 7.0 ‰ (Table 1). Additionally, the increase in $\delta\ ^{15}N$ is correlated with the increase in $^{40}Ar/^{36}Ar$ ratio (Fig. 5). Kaminakia and Ramos fumaroles, on the other hand, have more affinity with the atmospheric-like component and with a shallower environment condition (Figs. 2–5), as also suggested by the higher CH_4 contents (Table 1).

Both $^{40}Ar/^{36}Ar_{deep}$ and $^{3}He/^{4}He_{deep}$ ratio are akin to the global arc volcano range (Hilton et al., 2002). The $^{40}Ar/^{36}Ar_{deep}$ ratio is estimated at 551.6 ± 19.8, far less than the value of the upper mantle (35,000 ± 10,000; Table 2). This is a common feature observed along convergent plate margins, where the Ar isotopes in volcanic gases are thought to partly derive from an atmospheric source

Table 2
Ratios of the endmembers used and estimated through mixing modeling. The $^3He/^4He_{deep}$ ratio is constrained using the maximum value measured for the Nisyros fumaroles. $N_2/^3He$ and $N_2/^{36}Ar$ of the upper mantle is computed using $N_2/^4He$, $^3He/^4He$, $N_2/^{40}Ar$, and $^{40}Ar/^{36}Ar$ values available in literature. Ratios of the sediment endmember are reported in Sano et al. (2001) and are calculated using the highest $N_2/^{40}Ar$ (2.1×10^4) measured in siliceous sediments by Matsuo et al. (1978).

	Air	ASW	deep	upper mantle	sediment
$N_2/^4He$	1.49×10^5 [a]	2.64×10^5	31.8 ± 4.5	100 ± 50 [c]	1.05×10^4 [c]
$N_2/^3He$	1.07×10^{11}	1.9×10^{10}	3.66×10^6	$8.9^{+3.0}_{-3.8} \times 10^6$	1.4×10^{12} [h]
$N_2/^{36}Ar$	2.51×10^4	1.13×10^4	1.55×10^5 (1.64×10^6)	$5.3^{+4.2}_{-2.9} \times 10^6$	6×10^6 [h]
$N_2/^{40}Ar$	84	38	281.6 (479.6)	152 ± 58 [d]	2.1×10^4 [h]
$^4He/^{40}Ar$	5.61×10^{-4}	1.46×10^{-4}	8.85 (17.56)	2.0 ± 0.5 [e]	2 [a]
$^{40}Ar/^{36}Ar$	298.6 [b]	298.6	551.6 ± 19.8 (3,417 ± 239)	$3.5 \times 10^4 \pm 1 \times 10^4$ [e]	–
$^3He/^4He$ (Ra)	1	1	6.2	8 ± 1 [f]	0.02
$\delta^{15}N$	0	0	7 ± 3	−5 ± 2 [g]	7 ± 4 [h]

[a] Ozima and podosek (2002).
[b] Lee et al. (2006).
[c] Marty and Zimmermann (1999), Fischer et al. (2002), Elkins et al. (2006), and Caliro et al. (2015).
[d] Javoy and Pineau (1991), Marty and Zimmermann (1999),Cartigny et al. (2001).
[e] Burnard et al. (1997), Moreira et al. (1998), and Marty and Dauphas (2003).
[f] Farley and Neroda (1998).
[g] Marty and Dauphas (2003).
[h] Sano et al. (2001).

Table 3
Summary of the multiple linear regression model $N_2/^4He \times {}^{40}Ar/^{36}Ar = \widehat{\beta}_0 + \widehat{\beta}_1 \times {}^{40}Ar/^{36}Ar + \widehat{\beta}_2 \times N_2/^4He$ (mixing hyperbola in Fig. 3), showing the coefficients estimated by the method of least squares, the quantiles of the empirical population of residuals, and the goodness-of-fit expressed with the residual standard error (RSE) and the R^2. The table also displays the 95 % confidence interval of the coefficients, the standard error, the *t*-test statistics (t value) for the null-hypotheses and their corresponding two-sided P-values (Pr(>|t|)).

	Coefficient	95 % CI	Std. Error	t value	Pr(>|t|)
$\widehat{\beta}_0(q - x_0\, y_0)$	−8477	1547	789	−10.7	5.38E−09
$\widehat{\beta}_1(x_0)$	298.3	0.18	0.09	3173	1.64E−50
$\widehat{\beta}_2(y_0)$	31.8	4.5	2.3	13.8	1.14E−10
	Min.	1st Qu.	Median	3rd Qu.	Max.
Residuals	−442.1	−171.4	−17.9	199.1	426.8
RSE	253.3				
R^2	1.000				

Table 4
Summary of the linear regression model $^{36}Ar/^4He = \widehat{\beta}_0 + \widehat{\beta}_1 N_2/^4He$ (Fig. 4a, b), showing the coefficients estimated by the method of least squares, the quantiles of the empirical population of residuals, and a measure of fit expressed with the residual standard error (RSE) and the R^2. The table also reports the 95 % confidence interval of the coefficients, the standard error, the *t*-test statistics (t value) for the null-hypotheses and their corresponding two-sided P-values (Pr(>|t|)).

	Coefficient	95 % CI	Std. Error	t value	Pr(>|t|)
$\widehat{\beta}_0$	−1.12E−03	8.82E−05	4.50E−05	−24.9	2.08E−15
$\widehat{\beta}_1$	4.17E−05	1.09E−07	5.57E−08	748.6	6.75E−42
	Min.	1st Qu.	Median	3rd Qu.	Max.
Residuals	−2.69E−04	−1.37E−04	1.81E−05	7.61E−05	4.86E−04
RSE	1.77E−04				
R^2	1.000				

Table 5
Summary of the linear regression model $^{40}Ar/^{36}Ar = \widehat{\beta}_0 + \widehat{\beta}_1 N_2/^{36}Ar$ (Fig. 4c), showing the coefficients estimated by the method of least squares, the quantiles of the empirical population of residuals, and a measure of fit expressed with the residual standard error (RSE) and the R^2. The table also reports the 95 % confidence interval of the coefficients, the standard error, the *t*-test statistics (t value) for the null-hypotheses and their corresponding two-sided P-values (Pr(>|t|)).

	Coefficient	95 % CI	Std. Error	t value	Pr(>|t|)
$\widehat{\beta}_0$	251.6	6.2	3.2	79.1	2.45E−24
$\widehat{\beta}_1$	1.9E−03	1.4E−04	7E−05	27.1	4.73E−16
	Min.	1st Qu.	Median	3rd Qu.	Max.
Residuals	−9.96	−2.95	0.18	2.07	10.53
RSE	4.73				
R^2	0.976				

(Hilton et al., 2002). The addition of atmospheric Ar occurs in the mantle wedge through release of subduction components, and might also derive from the crust hosting the plumbing system (Hilton et al., 2002 and reference therein; Labidi and Young, 2022). About 98 % of the ^{36}Ar in the subducted slab is estimated to return into the atmosphere through arc volcano outgassing, with

an outflux of ~2.38 × 10^4 mol/year (Bekaert et al., 2021). The $^3He/^4He_{deep}$ ratio of 6.2 Ra unambiguously shows the magmatic origin of the deep component. This value is within the global arc volcanoes range of 7.4 ± 1.3 Ra (Sano and Fischer, 2013), which reflects additions of radiogenic ^4He from the crust (and lithospheric mantle) to a typical upper mantle source of 8 ± 1 Ra (Farley and Neroda, 1998). Since the maximum $^3He/^4He$ ratio measured along the SAVA is equal to 7.1 Ra (from Kolumbo submarine emissions), the Aegean mantle wedge presumably preserves the typical upper mantle ratio of ~8 Ra (Rizzo et al., 2016). Hence, the lower $^3He/^4He_{deep}$ ratio of Nisyros of 6.2 Ra reflects a relatively small contribution of crustal ^4He from the rocks hosting the plumbing system.

The $N_2/^{40}Ar_{deep}$ (281.6) and $N_2/^4He_{deep}$ (31.8) ratios are much lower than the typical values for arc volcanoes defined by most of the circum-Pacific systems (Fig. 2; grey band), with $N_2/^{40}Ar$ up to 2,000 and $N_2/^4He$ between 1000 and 10,000 (Giggenbach, 1991, 1996, 1997), or the gas emitted by other Mediterranean volcanoes (e.g., Vulcano, Campi Flegrei, and Milos), with N_2/He ratios of 400–800 (Giggenbach, 1997; Taran, 2011; Paonita et al., 2013; Caliro et al., 2014; light green band in Fig. 2). Gases released from arc volcanoes are generally characterized by higher N_2 contents relative to those of hot spots/divergent plate margins due to the incorporation of subducted sedimentary N in the mantle wedge (Matsuo et al., 1978; Kita et al., 1993). Nitrogen is predominantly fixed as NH_4^+ by biological processes and bound in seafloor sediments of the subducting slab (Barry and Hilton, 2016). Nisyros samples, on the other hand, spread towards a deep component located close to the He apex of the N_2-Ar-He ternary diagram (Fig. 2), which is common for mantle-derived magmas without input of sediments (Fig. 2). This mantle-like signature also appears when we investigate the source of the CO_2 in the $CO_2/^3He$ – $\delta^{13}C_{CO2}$ diagram (Fig. S6). Marini and Fiebig (2005) interpreted these low $N_2/^4He$, $N_2/^{40}Ar$, and $CO_2/^3He$ ratios in the gases of Nisyros as a sign of low N and C contents of sediments in either the subducting African plate or the rocks hosting the hydrothermal system. However, this hypothesis was formulated without considering nitrogen isotopes, which were not available for the SAVA gases so far.

The $\delta\ ^{15}N_{deep}$ (7 ± 3 ‰) value overlaps with the range of sediments recycled during subduction (7 ± 4 ‰; Fig. 5; Fischer et al., 2002; Sano et al., 1998, 2001). The high $\delta^{15}N$ of Nisyros gases (up to 7 ‰; Table 2) is comparable to that measured in gases emitted by other arc volcanoes, such as Momotombo (Nicaragua, up to 6.9 ‰; Elkins et al., 2006), Tecuamburro (Guatemala, 6.3 ± 0.3 ‰; Fischer et al., 2002), and Campi Flegrei (Italy, 6.3 ± 0.3 ‰; Caliro et al., 2014). Mixing calculations show that the magmatic (deep) endmember might derive ~85 % of its N from subducted sediment and ~15 % from the mantle (Fig. 5a, b; vertical purple arrow). A sediment endmember with $\delta\ ^{15}N$ of 7 (dark grey star) accounts for the isotopic signature of the analyzed gas samples except the two most positive ones (from Polyvotis Mikros), for which a heavier $\delta^{15}N$ source is required. To better fit the deep component, we

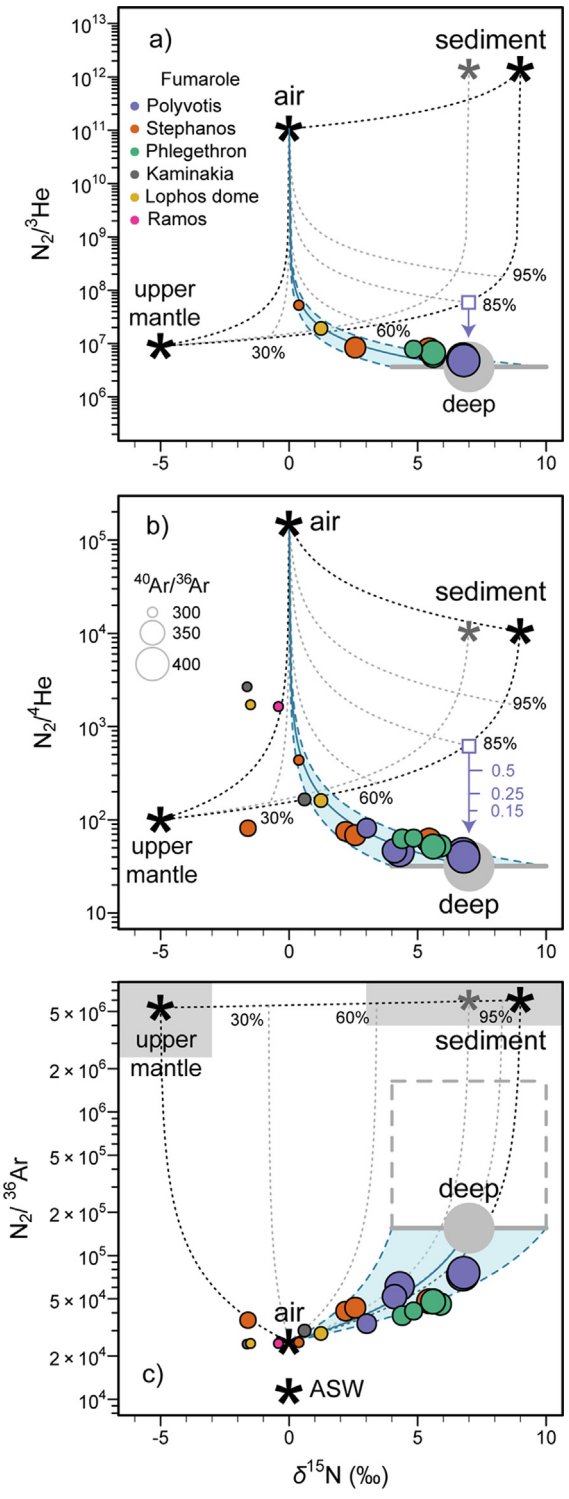

Fig. 5. $N_2/^3He$ (5a), $N_2/^4He$ (5b), and $N_2/^{36}Ar$ (5c) as a function of N isotopes (after Fischer et al., 2002; Sano et al., 1998, 2001). Upper mantle, sediment, air, and ASW (Table 2) are reported for comparison (black star). Ranges of upper mantle and sediment endmembers are also shown (grey box; 5c). Mixing curves between these endmembers are displayed as black dotted curves. The sediment endmember is fixed at $\delta\ ^{15}N$ = 9 ‰, but mixing of air and a hypothetical sediment with $\delta\ ^{15}N$ = 7 ‰ (smaller grey star) is also reported for comparison (gray dotted curve). Grey dotted curves reflect binary admixtures between air and air-free endmembers, constituted by relative proportions of sediment and upper mantle (numbers in % refer to sediment). Nisyros fumaroles are admixtures of air and a deep endmember (Table 2; light blue band). The size of the circles is proportional to the $^{40}Ar/^{36}Ar$ ratio. The deep endmember (grey circle) composition (Table 2) has been extrapolated from linear regression models using $N_2/^4He$ and $N_2/^{36}Ar$ ratios (Section 3.2.1, Figs. 3, 4). Nitrogen of the deep endmember mostly derives from subducted sediments, with a minor contribution from the upper mantle (85 % sediment and 15 % mantle using $N_2/^4He_{deep}$, 5b; 80 % sediment, 4 % mantle, and 16 % air using $N_2/^{36}Ar_{deep}$, 5c). The upper edge of the grey dashed box in 5c represents the maximum estimate of $N_2/^{36}Ar_{deep}$ (Table 2), resulting from $N_2/^4He$ = 27.3, that is the lower limit of the 95 % CI of $N_2/^4He_{deep}$ (Table 2). The low $N_2/^3He_{deep}$ and $N_2/^4He_{deep}$ ratios (5a, b) suggest that the deep endmember suffered solubility-controlled degassing. The Rayleigh fractionation trend and the residual gas fraction in a rhyodacitic melt with an initial $N_2/^4He$ = 600 (mean of the Mediterranean arc gas; white square) is displayed as a purple arrow (5b). (For interpretation of the references to colour in this figure legend, the reader is referred to the web version of this article.)

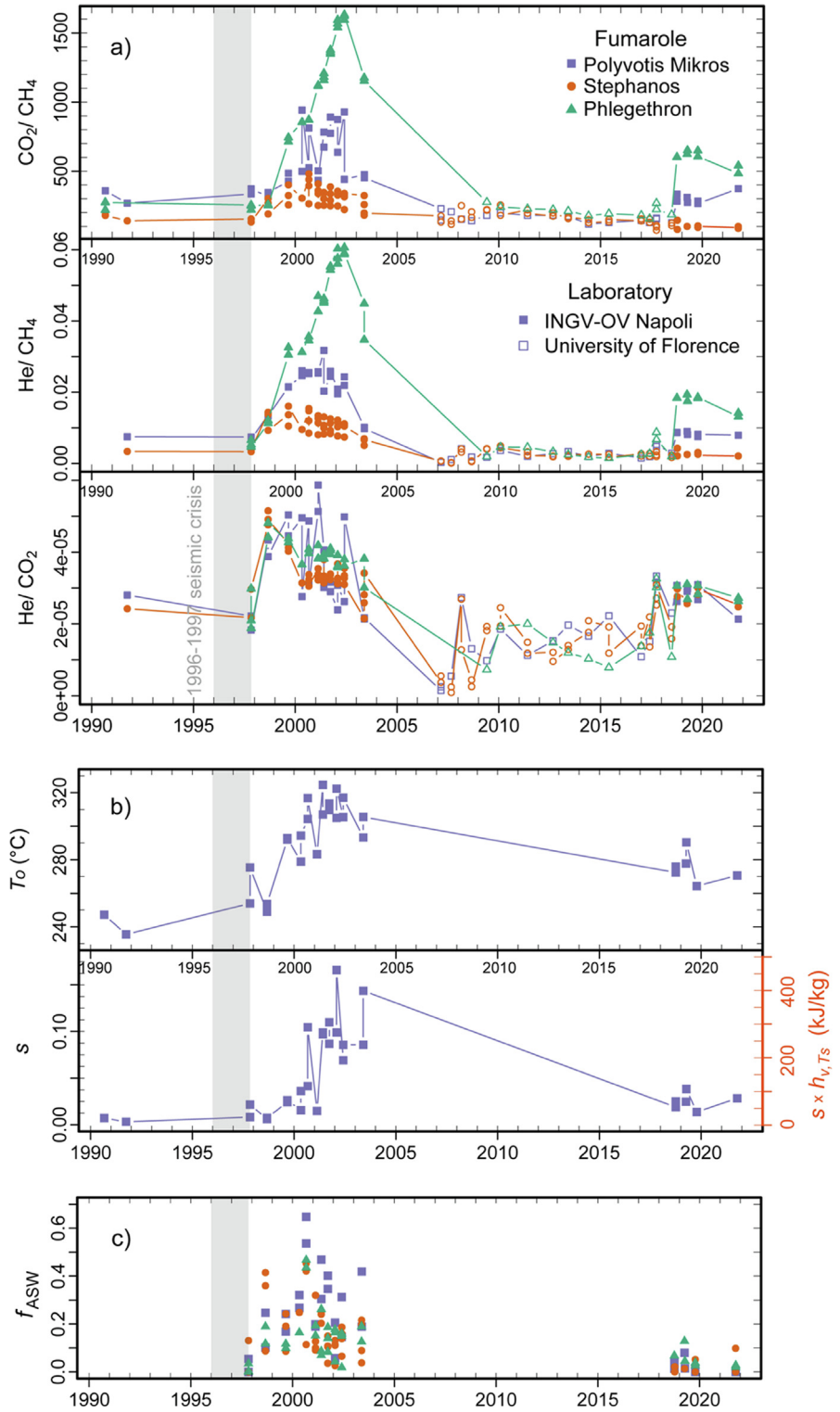

Fig. 6. Time series of CO_2/CH_4, He/CH_4, and He/CO_2 ratios measured in fumaroles (6a), equilibrium temperature of the hydrothermal liquid (To) and fraction of gas separated (s) through boiling (6b), and fraction of ASW (f_{ASW}; 6c). Closed symbols (6a) refer to the gas samples from Chiodini et al. (2002), Chiodini (2009) for 1990–2003 data and from this study for 2018–2021 data, which were all analyzed at the laboratory of the INGV-OV Napoli, whereas open symbols refer to 2007–2017 fumaroles analyzed at the Department of Earth Sciences of the University of Florence, Italy. All the parameters show a peak after the seismic crisis of 1996–1997, corresponding to increase in both magmatic species (He and CO_2) relative to hydrothermal species (CH_4; 6a), and in the temperature of the hydrothermal system and amount of vapor separated (6b,c). The dark orange axis in 6b shows the correspondent increase in the energy released from the hydrothermal system per kg of vapor separated through boiling. (For interpretation of the references to colour in this figure legend, the reader is referred to the web version of this article.)

would need a sediment endmember with $\delta^{15}N$ of ~9 ‰ (black star), which is reasonable if we consider that the subducted sedimentary materials have an *N*-isotopic signature between 3 and 11 ‰ (see the sediment grey box in Fig. 5c; Table 2). This predominant contribution of subducted sediment to the deep endmember composition is also shown in the $N_2/^{36}Ar$-$\delta^{15}N$ space (Fig. 5c), but it

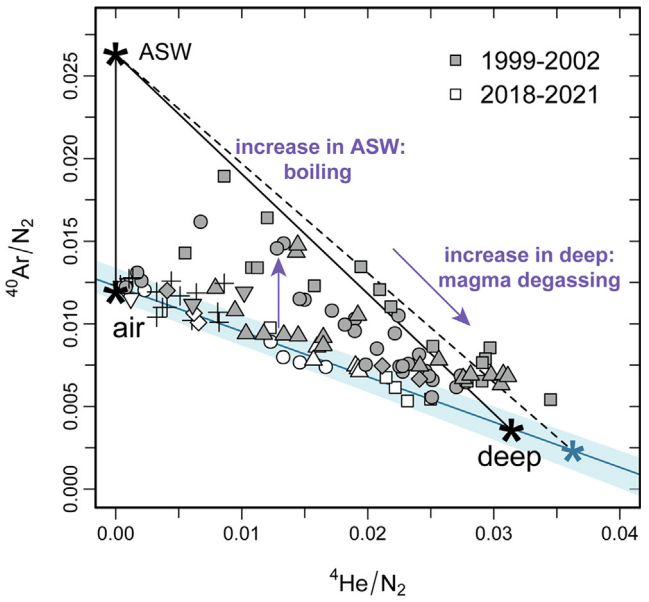

Fig. 7. $^{40}Ar/N_2$ as a function of $^4He/N_2$ in fumaroles collected after the seismic crisis (1999–2002, grey symbols) and from 2018 to 2021 (white symbols). These gases plot in a ternary mixing space defined by air, ASW, and the deep endmember (Table 2). The air-deep mixing line (blue) and its 95 % prediction band (light blue) is defined by linear regression on 2018–2021 data (this study). The dashed line reflects the ASW-deep mixing considering as deep endmember the lower limit of the 95 % CI of N_2/He_{deep}, that is 27.3, and N_2/Ar = 479.2 (Table 2; blue star). Samples collected after the seismic crisis show an increase in both f_{ASW} and f_{deep} (purple arrows). (For interpretation of the references to colour in this figure legend, the reader is referred to the web version of this article.)

requires a further addition of atmospheric ^{36}Ar to explain the low $N_2/^{36}Ar_{deep}$ ratio ($f_{sediment}$ = 80 %, f_{mantle} = 4 %, and f_{air} = 16 %; grey circle). Together with the $^{40}Ar/^{36}Ar_{deep}$ (551.6) ratio, the low $N_2/^{36}Ar_{deep}$ ratio may represent the evidence of atmospheric-Ar recycling in Nisyros magmas. However, the extent of this recycling could be smaller ($f_{air} \sim 1$ %) if we considered the maximum $N_2/^{36}Ar_{deep}$ of 1.64×10^6 (upper edge of the dashed grey box in Fig. 5c) and the correspondent maximum $^{40}Ar/^{36}Ar_{deep}$ of 3,417 – derived by choosing the lower limit of the 95 % CI of $N_2/^4He_{deep}$ (27.3) as predictor. In this case, the deep endmember would approach the composition of an air-free mixture of 95 % sediment and 5 % mantle. Despite the slightly different endmember proportions returned from these two approaches (Fig. 5b, c), N_2 of the deep component appears to be mostly originated from the Eastern Mediterranean Sea sediment subducted below the Aegean microplate with a minor contribution from the mantle wedge. However, the vertical shift in the $N_2/^3He_{deep}$ and $N_2/^4He_{deep}$ ratios (Fig. 5a, b) requires another physicochemical process affecting the composition of the deep endmember.

The $N_2/^4He_{deep}$ ratio is not only lower than the typical values for arc volcanoes (circum-Pacific) and Mediterranean arcs but also than that of the upper mantle (100 ± 50; Table 2), suggesting that Nisyros gases are affected by either a N_2 depletion or ^4He addition. The $N_2/^4He_{deep}$ ratio approaches the value of cratonic gases, such as those of the Kidd Creek Mine, Canada (5.1; Labidi et al., 2020), or intraplate volcanic gases, such as those of Yellowstone, USA (~80; Chiodini et al., 2012), which both result from the accumulation of crustal ^4He over billions of years (Lowenstern et al., 2014; Warr et al., 2018). Nevertheless, this is not the case of the Nisyros caldera, as the relatively high $^3He/^4He_{deep}$ ratio excludes the participation of a significant ^4He-rich crustal component. Hence, we suggest that the low $N_2/^4He_{deep}$ ratio is explained by a depletion in N_2, potentially through gas loss. Since He is more soluble than N_2 in silicate melts, N_2 is predominantly released during early-stage degassing from magma reservoirs at low crystallinity, which produces high N_2/He ratio (Giggenbach, 1996; Paonita, 2005). As crystallinity and volatile exsolution increase (during cooling and progressive solidification of the reservoir), the vapor phase produced by second boiling is expected to show a decreasing N_2/He ratio. Since N isotopes appear to be unaffected by fractionation during degassing (Fischer et al., 2005), the $\delta\ ^{15}N_{deep}$ value is expected to be preserved during the solubility-controlled reduction of the N_2/He ratio in the exsolved volatiles. Outgassing from a high-crystallinity magma reservoir is also supported by the high He/Ar_{deep} ratio (8.85; Table 2). Helium is about 10 times more soluble than Ar in silicate melts (Jambon et al., 1986; Marty and Zimmermann, 1999), and therefore high-crystallinity magmas should exsolve volatiles with high He/Ar ratios. On the contrary, magma degassing does not affect the N_2/Ar ratio, as N_2 and Ar show similar solubility (Miyazaki et al., 2004). The same process may also explain the low $CO_2/^3He$ ratio in Fig. S6, being CO_2 less soluble than He (Giggenbach, 1996).

To investigate the effect of magmatic outgassing on the $N_2/^4He_{deep}$ ratio, we performed Rayleigh fractionation calculations (Elkins et al., 2006) by modeling an open-system degassing in the form $N_2/^4He_{res} = N_2/^4He_i \times F^{(\alpha-1)/\alpha}$, where the elemental ratio in the residual melt ($N_2/^4He_{res}$) is a function of the ratio in the initial melt ($N_2/^4He_i$), the fraction of gas remaining in the melt (F), and the solubility ratio of the two species ($\alpha = S_{He}/S_{N2}$). Erupted products, petrological studies, and sulfur isotope modeling suggest the presence of a silicic (dacitic/rhyodacitic) upper-crustal reservoir below the Nisyros caldera, which formed through cooling and differentiation of mafic/intermediate magmas (Marini et al., 2002; Popa et al., 2019), fed from deeper down in the plumbing system. We calculate the solubility of He (S_{He}) and N_2 (S_{N2}) in a rhyodacitic magma with the model of Iacono-Marziano et al. (2010). This model returns the contents of He, Ar, and Ne in a dry melt, given its chemical composition, temperature, and pressure. To this end, we used the mean value of the Postcaldera domes (rhyodacites) as magma composition, T = 750 °C, and P = 200 MPa, as reported by Popa et al. (2019), and we assume that N_2 and Ar have the same solubility due to the very similar atomic radii (Miyazaki et al., 2004). Thus, S_{He} equal to 2.78 ccSTP/g, S_{N2} equal to 0.49 ccSTP/g, and the average $N_2/^4He$ ratio of the Mediterranean arc-gases (~600; Giggenbach, 1997) allowed us to calculate open-system degassing trends. These trends and the residual gas fraction in the melt are visualized as purple arrows in Figs. 2 and 5b. Notably, the $N_2/^4He_{deep}$ = 31.8 implies extensive degassing and a residual fraction of gas of only a few % (3 %). If we used the composition of a primitive magma (mafic enclaves in the Postcaldera domes; Popa et al., 2019) to simulate degassing trends from a mafic recharge, the residual gas fraction would not significantly change (~3.6 %). We are aware that a more accurate modeling that also includes the control of H_2O and CO_2 on noble gas solubilities (e.g., Nuccio and Paonita, 2001; Paonita et al., 2013) and the effect of chemical variations in the melt during differentiation is needed to better quantify magmatic degassing of multicomponent vapors. However, this degassing modeling is beyond the scope of this work and will be developed in future research.

5.2. N_2-He-Ar and reactive gas variation during the hydrothermal unrest following the 1996–1997 seismic crisis

Nisyros fumaroles show greater contributions from both ASW and deep magmatic endmembers after the 1996–1997 seismic crisis (Fig. 7; 1999–2002 samples, grey symbols). The increase in the f_{ASW} appears to be related to ASW or seawater (SW) circulating in the hydrothermal system rather than to shallow contamination (e.g., rain water). In fact, the 2018–2021 samples in Fig. 6c show a

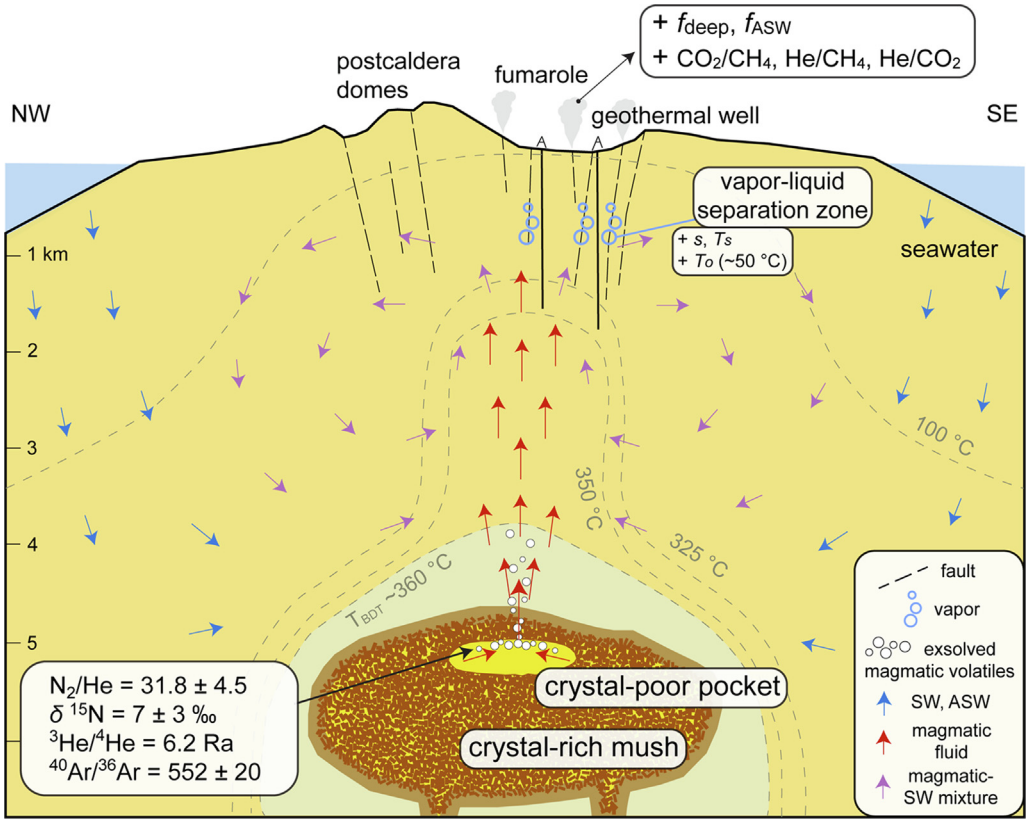

Fig. 8. Conceptual model of the magmatic-hydrothermal system of the Nisyros caldera during the episode of outgassing related to the 1996–1997 seismic crisis. The topography and the location of the faults and geothermal wells are taken from Dietrich et al. (2018). The upper-crustal part of the plumbing system of the Nisyros caldera consists of a silicic reservoir (dacitic/rhyodacitic) at high-crystallinity, differentiated from mafic magmas. The crystal-poor pocket of melt is a transient feature of magma reservoirs, and may not exist at present. Our data support the hypothesis of a high-crystallinity reservoir but the existence of this pocket and its potential volume and location cannot be easily determined without high resolution geophysical imaging. The grey contour surrounding the intrusion separates the hot ductile rocks (impermeable; greenish-gray) from the brittle (permeable; yellow) ones. We assume that the brittle-ductile transition (BDT) occurs in typical crustal rocks at ~360 °C (Hayba and Ingebritsen, 1997). Evolved magmatic fluids, whose composition has been estimated through N_2-He-Ar reverse mixing modeling (Table 2), accumulate in the mature silicic reservoir and are then injected into the overlying convective hydrothermal system. This addition of magmatic fluids causes an increase in the temperature of the hydrothermal system (~50 °C, reaching gas equilibrium temperature To of ~325 °C) and consequent boiling of deeper and peripheral parts, with an amount of vapor separated (s) about fifty times higher (vapor–liquid separation zone). These variations, together with the concurrent increase in f_{deep}, f_{ASW}, CO_2/CH_4, He/CH_4, and He/CO_2, are recorded at the surface in fumarolic fluids. (For interpretation of the references to colour in this figure legend, the reader is referred to the web version of this article.)

f_{ASW} by far lower than the 1999–2002 group, despite including those samples collected during rainy periods (April 2019). A sudden decompression induced by seismicity may have triggered gas exsolution from both shallow groundwater and deep ASW or SW in the hydrothermal system. However, such decompression is also expected to cause rapid variations in the fumarolic vents, whereas both ASW and the other parameters (Fig. 6) gradually change and reach a peak about two years after the earthquakes. The concurrent increase in *s* and *To* after the crisis (Fig. 6b) suggests that a greater amount of vapor separates through boiling from the hotter, deeper parts of the hydrothermal system. In particular, Polyvotis Mikros emissions indicate that reactive gases equilibrate at *To* ~ 50 °C higher in 1999–2002 (up to 325 °C versus ~275 °C in 2018–2021), and both the fraction of vapor separated and energy released through boiling increased by a factor of ~50 (Fig. 6b). This is also consistent with the higher fluxes of the fumaroles observed during the same period. The similar increase in the temperature of vapor–liquid separation (*Ts*, not shown in Fig. 6b) also suggests that the two-phase zone of the hydrothermal system (Fig. 8) extended towards greater depths during the unrest. The increase in ASW may therefore be explained by heating and boiling of both deeper and peripheral parts of the hydrothermal system.

The increment in magmatic species (CO_2 and He), relative to hydrothermal gas, (CH_4; Fig. 6a), and the increase in the f_{deep} (Fig. 7) after the crisis suggests that ascending magmatic fluids mix and heat the hydrothermal system, which in turn dissipate such excess of energy through boiling (as also hypothesized by Chiodini et al., 2002). Although the gas samples with greater f_{deep} plot outside the ternary admixture of Fig. 7 (solid lines), the composition of the deep magmatic endmember appears to be very similar for both periods (nowadays and after the seismic crisis). In fact, if we consider the lower limit of the 95 % CI of the $N_2/^4He_{deep}$ ratio (27.3; blue star), all the samples are contained in the triangle bounded by the ASW-deep dashed line (Fig. 7). In any case, a slightly different magmatic endmember after the seismic crisis would not change our interpretation, since it would still underscore an input of evolved magmatic gas with a low N_2/He ratio.

5.3. Implications for magma degassing

Magmatic fluids are thought to accumulate in magma reservoirs, as these cool and crystallize (Parmigiani et al., 2016; Edmonds and Wallace, 2017; Parmigiani et al., 2017; Degruyter et al., 2019), and are released towards the surface mostly in bursts of outgassing, as local overpressurization leads to brittle fracturing of the hot and typically impermeable ductile rocks surrounding the intrusion (Lamy-Chappuis et al., 2020). This accumulation of fluids, mostly occurring in crystal-poor pockets of highly evolved magmas

in the upper parts of reservoirs (Parmigiani et al., 2016), is favored by migration of exsolved volatiles in channel-like structures when magma reservoirs reach intermediate crystallinities (40–70 vol% crystals; Parmigiani et al., 2017; Degruyter et al., 2019). The low N_2/He_{deep} ratio may correspond to the residual gas phase formed through repeated episodes of volatile accumulation and expulsion during the differentiation of mafic to silicic magmas within the crustal plumbing system beneath the volcano. An episode of such gas expulsion is likely to be at the origin of the physicochemical variation observed in Nisyros fumaroles after the 1996–1997 seismic crisis.

To explain this episode of outgassing and the composition of the magmatic volatiles, we present a conceptual model of the magmatic-hydrothermal system of the Nisyros caldera (Fig. 8). Evolved magmatic fluids (low N_2/He), forming in a mature silicic reservoir in the upper crust (~1.5–2 kbar; Popa et al., 2019; Huber et al., 2019), are injected into the hydrothermal system and are recorded at the surface between 1999 and 2002 (Figs. 6a, 7). Further support to this late-stage outgassing event from a high-crystallinity reservoir comes from a spike in the He/CO_2 ratio observed in the fumaroles in the same period (Fig. 6a). Possible contributions from low $N_2/^4He$, degassed mafic magmas from the deeper parts of the plumbing system cannot be excluded. In any case, the inferred state of the reservoir (high average crystallinity) and its relative (late) stage of degassing would not change, as partial degassing calculations (Section 5.1) return almost the same residual gas fraction in both mafic and silicic magmas with $N_2/^4He_{res}$ ~32. If the gases were derived from a low-crystallinity magma, for example, after a new mafic recharge, we should expect higher N_2/He and lower He/CO_2 ratios. This process is well-documented in the time series of Campi Flegrei (Italy), where after a new mafic recharge during the 1982–1984 bradyseism, fumarole N_2/He ratios increased up to 800 and gradually decreased down to 200 (Caliro et al., 2014; Buono et al., 2022).

Once the released magmatic volatiles enter the brittle region above the magma reservoir, fractures enable their transfer in the convective hydrothermal system, where they mix and heat pre-existing fluids. Considering the delay between the fumarolic chemical changes and the earthquakes at Nisyros (Fig. 6), we suggest that the timescale of magmatic fluid upflow is about two years. This timescale depends on both the different fluid mobility between the ductile and brittle domain and the presence of the hydrothermal system. Nowadays, the fumarolic vents of Nisyros show lower fraction of the deep endmember and pre-seismic crisis physicochemical conditions (Figs. 6, 7) due to outgassing, mixing, and convection in the hydrothermal system over the last twenty years. Nevertheless, potential diffusion of volatiles from the magma chamber (i.e., passive outgassing) after this episode of outgassing cannot be ruled out, although we assume that this process should be limited.

6. Conclusions

Reverse mixing modeling of N_2, He, and Ar reveals that the current hydrothermal fluids emitted from the Nisyros caldera are a mixture of an atmospheric-like component and a deep, magmatic endmember. We suggest that this deep endmember represents magmatic fluids typical of subduction zones, although their chemical composition also depends on the state of the magma chamber (in particular its average crystallinity) and on its relative stage of degassing. Evidence of arc-type fluids mainly derives from He and N isotope ratios. The $^3He/^4He_{deep}$ ratio (6.2 Ra) is linked to the local magmatic source, while $\delta^{15}N_{deep}$ (7 ± 3 ‰) indicates the contribution of the subducted Eastern Mediterranean Sea sediment. We interpret the low N_2/He ratio relative to the typical circum-Pacific and Mediterranean range of arc volcanoes as a solubility-controlled differential outgassing rather than an absence of sediments on the subducted slab, as previously proposed (see Marini and Fiebig, 2005). This N_2-depleted gas likely exsolved from a silicic magma stored at shallow depth below the Nisyros caldera, and some of it escapes the reservoir during episodes of outgassing. The last major outgassing event was favored by the 1996–1997 seismic crisis and was recorded by significant compositional changes in the fumarolic gas discharges between 1999 and 2002 (Fig. 8). These variations also affected the N_2-He-Ar system, as shown by reverse mixing modeling. The approach described in this work has therefore important ramifications for volcano monitoring, as it enables us not only to identify the magmatic gas signature during periods of dormancy, but also to better understand magma outgassing episodes and the state of magma reservoirs beneath active volcanoes.

Data availability

The data are shared as Supplementary Material

Declaration of Competing Interest

The authors declare that they have no known competing financial interests or personal relationships that could have appeared to influence the work reported in this paper.

Acknowledgments

This research was supported by the Swiss National Science Foundation grant 200021_178928 to OB. We thank Francesco Capecchiacci, Alessandro Santi, and Emilio Cuoco for their help during fumarole sampling and gas analyses at INGV-OV and University of Florence (Italy), and Mariano Tantillo for the analyses of noble gas isotopes at INGV-PA. We also thank Razvan-Gabriel Popa for fruitful discussions. We would like to thank Tobias Fischer and two anonymous reviewers for their constructive comments that improved this manuscript, and Manuel Moreira for editorial handling.

Appendix A. Supplementary material

The Supplementary Material includes a basic statistical description of the method of least squares used to solve the three coefficients (the two asymptotes x_0 and y_0, and the curvature factor q) of the binary mixing hyperbola in the $N_2/^4He$-$^{40}Ar/^{36}Ar$ space. This file also includes the following supplementary figures: (S1–S3) Tukey-Anscombe plots, (S4) gas equilibria in the H_2O-H_2-CO-CO_2-CH_4 system, (S5) δD-H_2O versus $\delta^{18}O$-H_2O in steam condensates, and (S6) $CO_2/^3He$ versus $\delta^{13}C_{CO2}$ in fumaroles. Research Data includes chemical and isotopic compositions of the fumaroles (Table 1.csv), CO_2/CH_4, He/CH_4, and He/CO_2 time series (Time series.csv), an R script to calculate the compositions of the endmembers using the mixing hyperbola method (Hyperbola_function.R), and a table with Nisyros $N_2/^4He$ and $^{40}Ar/^{36}Ar$ data to read in the R script (Hyperbola_data.csv). Supplementary material to this article can be found online at https://doi.org/10.1016/j.gca.2022.08.028.

References

Albarède, F., 1995. Introduction to Geochemical Modeling. Cambridge University Press, Cambridge.

Bachmann, O., Deering, C.D., Ruprecht, J.S., Huber, C., Skopelitis, A., Schnyder, C., 2012. Evolution of silicic magmas in the Kos-Nisyros volcanic center, Greece: a petrological cycle associated with caldera collapse. Contrib. Miner. Petrol. 163, 151–166.

Bachmann, O., Allen, S.R., Bouvet de Maisonneuve, C., 2019. The Kos–Nisyros–Yali Volcanic Field. Elements 15, 191–196.

Barry, P.H., Hilton, D.R., 2016. Release of subducted sedimentary nitrogen throughout Earth's mantle. Geochem. Perspect. Lett., 148–159

Bebout, G.E., Fogel, M.L., 1992. Nitrogen-isotope compositions of metasedimentary rocks in the Catalina Schist, California: implications for metamorphic devolatilization history. Geochim. Cosmochim. Acta 56, 2839–2849.
Bekaert, D.V., Turner, S.J., Broadley, M.W., Barnes, J.D., Halldórsson, S.A., Labidi, J., Wade, J., Walowski, K.J., Barry, P.H., 2021. Subduction-driven volatile recycling: A global mass balance. Annu. Rev. Earth Planet. Sci. 49, 37–70.
Bini, G., Chiodini, G., Cardellini, C., Vougioukalakis, G.E., Bachmann, O., 2019. Diffuse emission of CO_2 and convective heat release at Nisyros caldera (Greece). J. Volcanol. Geoth. Res. 376, 44–53.
Bini, G., Chiodini, G., Lucchetti, C., Moschini, P., Caliro, S., Mollo, S., Selva, J., Tuccimei, P., Galli, G., Bachmann, O., 2020. Deep versus shallow sources of CO_2 and Rn from a multi-parametric approach: the case of the Nisyros caldera (Aegean Arc, Greece). Sci. Rep. 10, 13782.
Brombach, T., Caliro, S., Chiodini, G., Fiebig, J., Hunziker, J.C., Raco, B., 2003. Geochemical evidence for mixing of magmatic fluids with seawater, Nisyros hydrothermal system, Greece. Bull. Volcanol. 65, 505–516.
Buono, G., Paonita, A., Pappalardo, L., Caliro, S., Tramelli, A., Chiodini, G., 2022. New insights into the recent magma dynamics under Campi Flegrei caldera (Italy) from petrological and geochemical evidence. J. Geophys. Res.: Solid Earth 127. e2021JB023773.
Burnard, P., Graham, D., Turner, G., 1997. Vesicle-specific noble gas analyses of "popping rock": implications for primordial noble gases in Earth. Science 276, 568–571.
Caliro, S., Chiodini, G., Galluzzo, D., Granieri, D., La Rocca, M., Saccorotti, G., Ventura, G., 2005. Recent activity of Nisyros volcano (Greece) inferred from structural, geochemical and seismological data. Bull. Volcanol. 67, 358–369.
Caliro, S., Chiodini, G., Paonita, A., 2014. Geochemical evidences of magma dynamics at Campi Flegrei (Italy). Geochim. Cosmochim. Acta 132, 1–15.
Caliro, S., Viveiros, F., Chiodini, G., Ferreira, T., 2015. Gas geochemistry of hydrothermal fluids of the S. Miguel and Terceira Islands, Azores. Geochim. Cosmochim. Acta 168, 43–57.
Caracausi, A., Italiano, F., Paonita, A., Rizzo, A., Nuccio, P.M., 2003. Evidence of deep magma degassing and ascent by geochemistry of peripheral gas emissions at Mount Etna (Italy): Assessment of the magmatic reservoir pressure. J. Geophys. Res. Solid Earth 108 (B10).
Cartigny, P., Jendrzejewski, N., Pineau, F., Petit, E., Javoy, M., 2001. Volatile (C, N, Ar) variability in MORB and the respective roles of mantle source heterogeneity and degassing: the case of the Southwest Indian Ridge. Earth Planet. Sci. Lett. 194, 241–257.
Chiodini, G., 2009. CO_2/CH_4 ratio in fumaroles a powerful tool to detect magma degassing episodes at quiescent volcanoes. Geophys. Res. Lett. 36 (2).
Chiodini, G., Cioni, R., Leonis, C., Marini, L., Raco, B., 1993. Fluid geochemistry of Nisyros island, Dodecanese, Greece. J. Volcanol. Geotherm. Res. 56, 95–112.
Chiodini, G., Marini, L., 1998. Hydrothermal gas equilibria: the H_2O-H_2-CO_2-CO-CH_4 system. Geochim. Cosmochim. Acta 62, 2673–2687.
Chiodini, G., Brombach, T., Caliro, S., Cardellini, C., Marini, L., Dietrich, V., 2002. Geochemical indicators of possible ongoing volcanic unrest at Nisyros Island (Greece). Geophys. Res. Lett. 29 (16), 1759.
Chiodini, G., Caliro, S., Caramanna, G., Granieri, D., Minopoli, C., Moretti, R., Perotta, L., Ventura, G., 2006. Geochemistry of the Submarine Gaseous Emissions of Panarea (Aeolian Islands, Southern Italy): Magmatic vs. Hydrothermal Origin and Implications for Volcanic Surveillance. Pure Appl. Geophys. 163, 759–780.
Chiodini, G., Caliro, S., Lowenstern, J.B., Evans, W.C., Bergfeld, D., Tassi, F., Tedesco, D., 2012. Insights from fumarole gas geochemistry on the origin of hydrothermal fluids on the Yellowstone Plateau. Geochim. Cosmochim. Acta 89, 265–278.
Chiodini, G., Vandemeulebrouck, J., Caliro, S., D'Auria, L., De Martino, P., Mangiacapra, A., Petrillo, Z., 2015. Evidence of thermal-driven processes triggering the 2005–2014 unrest at Campi Flegrei caldera. Earth Planet. Sci. Lett. 414, 58–67.
Chiodini, G., Caliro, S., Avino, R., Bini, G., Giudicepietro, F., De Cesare, W., Ricciolino, P., Aiuppa, A., Cardellini, C., Petrillo, Z., Selva, J., Siniscalchi, A., Tripaldi, S., 2021. Hydrothermal pressure-temperature control on CO2 emissions and seismicity at Campi Flegrei (Italy). J. Volcanol. Geoth. Res. 414, 107245.
Degruyter, W., Parmigiani, A., Huber, C., Bachmann, O., 2019. How do volatiles escape their shallow magmatic hearth? Phil. Trans. R. Soc. A 377, 20180017.
Di Paola, G.M., 1974. Volcanology and petrology of Nisyros Island (Dodecanese, Greece). Bull. Volcanol. 38, 944–987.
Dietrich, V.J., Chiodini, G., Schwandner, F.M., 2018. The hydrothermal system and geothermal activity. In: Dietrich, V.J., Lagios, E. (Eds.), Nisyros Volcano. Springer, Cham, pp. 145–201.
Edmonds, M., Wallace, P.J., 2017. Volatile and exsolved vapor in volcanic systems. Elements 13, 29–34.
Elkins, L.J., Fischer, T.P., Hilton, D.R., Sharp, Z.D., McKnight, S., Walker, J., 2006. Tracing nitrogen in volcanic and geothermal volatiles from the Nicaraguan volcanic front. Geochim. Cosmochim. Acta 70, 5215–5235.
Farley, K.A., Neroda, E., 1998. Noble gases in the earth's mantle. Annu. Rev. Earth Planet. Sci. 26 (1), 189–218.
Fiebig, J., Chiodini, G., Caliro, S., Rizzo, A., Spangenberg, J., Hunziker, J.C., 2004. Chemical and isotopic equilibrium between CO_2 and CH_4 in fumarolic gas discharges: Generation of CH_4 in arc magmatic-hydrothermal systems. Geochim. Cosmochim. Acta 68, 2321–2334.
Fischer, T.P., Hilton, D.R., Zimmer, M.M., Shaw, A.M., Sharp, Z.D., Walker, J.A., 2002. Subduction and Recycling of Nitrogen Along the Central American Margin. Science 297, 1154–1157.
Fischer, T.P., Takahata, N., Sano, Y., Sumino, H., Hilton, D.R., 2005. Nitrogen isotopes of the mantle: Insights from mineral separates. Geophys. Res. Lett. 32, L11305.
Francalanci, L., Varekamp, J.C., Vougioukalakis, G., Delant, M.J., Innocenti, F., Manetti, P., 1995. Crystal retention, fractionation and crustal assimilation in a convecting magma chamber, Nisyros Volcano, Greece. Bull. Volcanol. 56, 601–620.
Giggenbach, W.F., 1975. A simple method for the collection and analysis of volcanic gas samples. Bull. Volcanol. 39, 132–145.
Giggenbach, W.F., 1987. Redox processes governing the chemistry of fumarolic gas discharges from White Island, New Zealand. Appl. Geochem. 2, 143–161.
Giggenbach, W.F., 1991. Chemical techniques in geothermal exploration. In: D'Amore, F. (Ed.), Application of Geochemistry in Geothermal Reservoir Development. UNITAR, Rome, pp. 119–144.
Giggenbach, W.F., 1992. Isotopic shifts in waters from geothermal and volcanic systems along convergent plate boundaries and their origin. Earth Planet. Sci. Lett. 113, 495–510.
Giggenbach, W.F., 1996. Chemical composition of volcanic gases. In: Scarpa, R., Tilling, R.I. (Eds.), Monitoring and Mitigation of Volcano Hazards. Springer, Berlin, Heidelberg, pp. 221–256.
Giggenbach, W.F., 1997. The origin and evolution of fluids in magmatic-hydrothermal systems. In: Barnes, H.L. (Ed.), Geochemistry of Hydrothermal Ore Deposits. John Wiley & Sons, pp. 737–796.
Giggenbach, W.F., Goguel, R.L., 1989. Collection and analysis of geothermal and volcanic water and gas discharges. Report No. CD 2401. Chemistry Division, DSIR, Petone, New Zealand.
Giggenbach, W.F., Matsuo, S., 1991. Evaluation of results from Second and Third IAVCEI Field Workshops on Volcanic Gases, Mt Usu, Japan, and White Island, New Zealand. Appl. Geochem. 6, 125–141.
Gottsmann, J., Carniel, R., Coppo, N., Wooller, L., Hautmann, S., Rymer, H., 2007. Oscillations in hydrothermal systems as a source of periodic unrest at caldera volcanoes: Multiparameter insights from Nisyros, Greece. Geophys. Res. Lett. 34, L07307.
Hautmann, S., Gottsmann, J., 2018. Ground Deformation and Gravity Changes of the Kos-Nisyros Volcanic System Between 1995 and 2008. In: Dietrich, V.J., Lagios, E. (Eds.), Nisyros Volcano. Active Volcanoes of the World. Springer International Publishing, Cham, pp. 303–319.
Hayba, D.O., Ingebritsen, S.E., 1997. Multiphase groundwater flow near cooling plutons. J. Geophys. Res. Solid Earth 102, 12235–12252.
Hernández, P.A., Melián, G.V., Asensio-Ramos, M., Padrón, E., Sumino, H., Pérez, N. M., Padilla, G.D., Barrancos, J., Rodríguez, F., Amonte, C., Arcilla, C., Lagmay, A.M., 2021. Geochemical and isotopic evidence of volcanic plumbing system processes from fumarolic gases of Taal volcano, Philippines, prior to the January 2020 eruption. Chem. Geol. 574, 120216.
Hilton, D.R., Fischer, T.P., Marty, B., 2002. Noble Gases and Volatile Recycling at Subduction Zones. Rev. Mineral. Geochem. 47, 319–370.
Huber, C., Townsend, M., Degruyter, W., Bachmann, O., 2019. Optimal depth of subvolcanic magma chamber growth controlled by volatiles and crust rheology. Nat. Geosci. 12, 762–768.
Iacono-Marziano, G., Paonita, A., Rizzo, A., Scaillet, B., Gaillard, F., 2010. Noble gas solubilities in silicate melts: New experimental results and a comprehensive model of the effects of liquid composition, temperature and pressure. Chem. Geol. 279, 145–157.
Jambon, A., Weber, H., Braun, O., 1986. Solubility of He, Ne, Ar, Kr and Xe in a basalt melt in the range 1250–1600 C. Geochemical implications. Geochim. Cosmochim. Acta 50, 401–408.
Janoušek, V., Moyen, J.-F., Martin, H., Erban, V., Farrow, C., 2016. Geochemical Modelling of Igneous Processes – Principles And Recipes in R Language. Springer, Berlin Heidelberg, Berlin, Heidelberg.
Javoy, M., Pineau, F., 1991. The volatiles record of a "popping" rock from the Mid-Atlantic Ridge at 14 N: chemical and isotopic composition of gas trapped in the vesicles. Earth Planet. Sci. Lett. 107, 598–611.
Jolivet, L., Faccenna, C., Huet, B., Labrousse, L., Le Pourhiet, L., Lacombe, O., Lecomte, E., Burov, E., Denèle, Y., Brun, J.-P., Philippon, M., Paul, A., Salaün, G., Karabulut, H., Piromallo, C., Monié, P., Gueydan, F., Okay, A.I., Oberhänsli, R., Pourteau, A., Augier, R., Gadenne, L., Driussi, O., 2013. Aegean tectonics: Strain localisation, slab tearing and trench retreat. Tectonophysics 597–598, 1–33.
Kita, I., Nitta, K., Nagao, K., Taguchi, S., Koga, A., 1993. Difference in N_2/Ar ratio of magmatic gases from northeast and southwest Japan: New evidence for different states of plate subduction. Geology 21, 391–394.
Klaver, M., Djuly, T., de Graaf, S., Sakes, A., Wijbrans, J., Davies, G., Vroon, P., 2015. Temporal and spatial variations in provenance of Eastern Mediterranean Sea sediments: Implications for Aegean and Aeolian arc volcanism. Geochim. Cosmochim. Acta 153, 149–168.
Klaver, M., Davies, G.R., Vroon, P.Z., 2016. Subslab mantle of African provenance infiltrating the Aegean mantle wedge. Geology 44, 367–370.
Kopf, A., 2003. The Mediterranean Ridge: A mass balance across the fastest growing accretionary complex on Earth. J. Geophys. Res. 108, 2372.
Labanieh, S., Chauvel, C., Germa, A., Quidelleur, X., Lewin, E., 2010. Isotopic hyperbolas constrain sources and processes under the Lesser Antilles arc. Earth Planet. Sci. Lett. 298, 35–46.
Labidi, J., Barry, P.H., Bekaert, D.V., Broadley, M.W., Marty, B., Giunta, T., Warr, O., Sherwood, L.B., Fischer, T.P., Avice, G., Caracausi, A., Ballentine, C.J., Halldórsson, S.A., Stefánsson, A., Kurz, M.D., Kohl, I.E., Young, E.D., 2020. Hydrothermal 15N15N abundances constrain the origins of mantle nitrogen. Nature 580, 367–371.

Labidi, J., Young, E.D., 2022. The origin and dynamics of nitrogen in the Earth's mantle constrained by 15N15N in hydrothermal gases. Chem. Geol. 591, 120709.
Lagios, E., Sakkas, V., Is, P., Dietrich, V., 2005. Ground deformation of Nisyros Volcano (Greece) for the period 1995–2002: Results from DInSAR and DGPS observations. Bull. Volcanol. 68, 201–214.
Lamy-Chappuis, B., Heinrich, C.A., Driesner, T., Weis, P., 2020. Mechanisms and patterns of magmatic fluid transport in cooling hydrous intrusions. Earth Planet. Sci. Lett. 535, 116111.
Langmuir, C.H., Vocke, R.D., Hanson, G.N., Hart, S.R., 1978. A general mixing equation with applications to Icelandic basalts. Earth Planet. Sci. Lett. 37, 380–392.
Lee, J.-Y., Marti, K., Severinghaus, J.P., Kawamura, K., Yoo, H.-S., Lee, J.B., Kim, J.S., 2006. A redetermination of the isotopic abundances of atmospheric Ar. Geochim. Cosmochim. Acta 70, 4507–4512.
Lowenstern, J.B., Evans, W.C., Bergfeld, D., Hunt, A.G., 2014. Prodigious degassing of a billion years of accumulated radiogenic helium at Yellowstone. Nature 506, 355–358.
Marini, L., Fiebig, J., 2005. Fluid geochemistry of the magmatic-hydrothermal system of Nisyros (Greece). In: Hunziker, J.C., Marini, L. (Eds.), The Geology, Geochemistry and Evolution of Nisyros Volcano (Greece). Implications for the Volcanic Hazards. Memoires de Géologie, Lausanne, pp. 121–163.
Marini, L., Principe, C., Chiodini, G., Cioni, R., Fytikas, M., Marinelli, G., 1993. Hydrothermal eruptions of Nisyros (Dodecanese, Greece). Past events and present hazard. J. Volcanol. Geoth. Res. 56, 71–94.
Marini, L., Gambardella, B., Principe, C., Arias, A., Brombach, T., Hunziker, J.C., 2002. Characterization of magmatic sulfur in the Aegean island arc by means of the $\delta^{34}S$ values of fumarolic H_2S, elemental S, and hydrothermal gypsum from Nisyros and Milos Islands. Earth Planet. Sci. Lett. 200, 15–31.
Marty, B., Dauphas, N., 2003. The nitrogen record of crust–mantle interaction and mantle convection from Archean to Present. Earth Planet. Sci. Lett. 206, 397–410.
Marty, B., Zimmermann, L., 1999. Volatiles (He, C, N, Ar) in mid-ocean ridge basalts: assessment of shallow-level fractionation and characterization of source composition. Geochim. Cosmochim. Acta 63, 3619–3633.
Matsuo, S., Suzuki, M., Mizutani, Y., 1978. Nitrogen to argon ratio in volcanic gases. Adv. Earth Planet. Sci. 3, 17–25.
Miyazaki, A., Hiyagon, H., Sugiura, N., Hirose, K., Takahashi, E., 2004. Solubilities of nitrogen and noble gases in silicate melts under various oxygen fugacities: implications for the origin and degassing history of nitrogen and noble gases in the earth. Geochim. Cosmochim. Acta 68, 387–401.
Moreira, M., Kunz, J., Allègre, C., 1998. Rare Gas Systematics in Popping Rock: Isotopic and Elemental Compositions in the Upper Mantle. Science 279, 1178–1181.
Moretti, R., Komorowski, J.-C., Ucciani, G., Moune, S., Jessop, D., de Chabalier, J.-B., Beauducel, F., Bonifacie, M., Burtin, A., Vallée, M., Deroussi, S., Robert, V., Gibert, D., Didier, T., Kitou, T., Feuillet, N., Allard, P., Tamburello, G., Shreve, T., Saurel, J.-M., Lemarchand, A., Rosas-Carbajal, M., Agrinier, P., Le Friant, A., Chaussidon, M., 2020. The 2018 unrest phase at La Soufrière of Guadeloupe (French West Indies) andesitic volcano: Scrutiny of a failed but prodromal phreatic eruption. J. Volcanol. Geoth. Res. 393, 106769.
Nuccio, P.M., Paonita, A., 2001. Magmatic degassing of multicomponent vapors and assessment of magma depth: application to Vulcano Island (Italy). Earth Planet. Sci. Lett. 193, 467–481.
Ozima, M., Podosek, F.A., 2002. Noble Gas Geochemistry. Cambridge University Press.
Paonita, A., 2005. Noble gas solubility in silicate melts: a review of experimentation and theory, and implications regarding magma degassing processes. Ann. Geophys. 48, 647–669.
Paonita, A., Federico, C., Bonfanti, P., Capasso, G., Inguaggiato, S., Italiano, F., Madonia, P., Pecoraino, G., Sortino, F., 2013. The episodic and abrupt geochemical changes at La Fossa fumaroles (Vulcano Island, Italy) and related constraints on the dynamics, structure, and compositions of the magmatic system. Geochim. Cosmochim. Acta 120, 158–178.
Papadopoulos, G.A., Sachpazi, M., Panopoulou, G., Stavrakakis, G., 1998. The volcanoseismic crisis of 1996–97 in Nisyros, SE Aegean Sea, Greece. Terra Nova 10, 151–154.
Parmigiani, A., Faroughi, S., Huber, C., Bachmann, O., Su, Y., 2016. Bubble accumulation and its role in the evolution of magma reservoirs in the upper crust. Nature 532, 492–495.
Parmigiani, A., Degruyter, W., Leclaire, S., Huber, C., Bachmann, O., 2017. The mechanics of shallow magma reservoir outgassing. Geochem. Geophys. Geosystems 18, 2887–2905.
Peters, K.E., Sweeney, R.E., Kaplan, I.R., 1978. Correlation of carbon and nitrogen stable isotope ratios in sedimentary organic matter 1. Limnol. Oceanogr. 23, 598–604.
Popa, R.-G., Bachmann, O., Ellis, B.S., Degruyter, W., Tollan, P., Kyriakopoulos, K., 2019. A connection between magma chamber processes and eruptive styles revealed at Nisyros-Yali volcano (Greece). J. Volcanol. Geoth. Res. 387, 106666.
Popa, R.-G., Guillong, M., Bachmann, O., Szymanowski, D., Ellis, B., 2020. U-Th zircon dating reveals a correlation between eruptive styles and repose periods at the Nisyros-Yali volcanic area, Greece. Chem. Geol. 555, 119830.
R Core Team, 2022. R: A Language and Environment for Statistical Computing. R Foundation for Statistical Computing, Vienna, Austria. https://www.R-project.org/.
Rizzo, A.L., Barberi, F., Carapezza, M.L., Di Piazza, A., Francalanci, L., Sortino, F., D'Alessandro, W., 2015. New mafic magma refilling a quiescent volcano: Evidence from He-Ne-Ar isotopes during the 2011–2012 unrest at Santorini, Greece. Geochem. Geophys. Geosyst. 16, 798–814.
Rizzo, A.L., Caracausi, A., Chavagnac, V., Nomikou, P., Polymenakou, P., Mandalakis, M., Kotoulas, G., Magoulas, A., Castillo, A., Lampridou, D., 2016. Kolumbo submarine volcano (Greece): An active window into the Aegean subduction system. Sci. Rep. 6, 28013.
Rouwet, D., Sandri, L., Marzocchi, W., Gottsmann, J., Selva, J., Tonini, R., Papale, P., 2014. Recognizing and tracking volcanic hazards related to non-magmatic unrest: a review. J. Appl. Volcanol. 3, 17.
Sano, Y., Fischer, T.P., 2013. The analysis and interpretation of noble gases in modern hydrothermal systems. In: Burnard, P. (Ed.), The Noble Gases as Geochemical Tracers. Springer, Berlin, Heidelberg, pp. 249–317.
Sano, Y., Takahata, N., Nishio, Y., Marty, B., 1998. Nitrogen recycling in subduction zones. Geophys. Res. Lett. 25, 2289–2292.
Sano, Y., Takahata, N., Nishio, Y., Fischer, T.P., Williams, S.N., 2001. Volcanic flux of nitrogen from the Earth. Chem. Geol. 171, 263–271.
Sano, Y., Wakita, H., 1985. Geographical distribution of $^3He/^4He$ ratios in Japan: Implications for arc tectonics and incipient magmatism. J. Geophys. Res. Solid Earth 90, 8729–8741.
Scott, S., Driesner, T., Weis, P., 2015. Geologic controls on supercritical geothermal resources above magmatic intrusions. Nat. Commun. 6, 7837.
Shimizu, A., Sumino, H., Nagao, K., Notsu, K., Mitropoulos, P., 2005. Variation in noble gas isotopic composition of gas samples from the Aegean arc, Greece. J. Volcanol. Geotherm. Res. 140, 321–339.
Sorey, M.L., Evans, W.C., Kennedy, B.M., Farrar, C.D., Hainsworth, L.J., Hausback, B., 1998. Carbon dioxide and helium emissions from a reservoir of magmatic gas beneath Mammoth Mountain, California. J. Geophys. Res. Solid Earth 103, 15303–15323.
Sykioti, O., Kontoes, C.C., Elias, P., Briole, P., Sachpazi, M., Paradissis, D., Kotsis, I., 2003. Ground deformation at Nisyros volcano (Greece) detected by ERS-2 SAR differential interferometry. Int. J. Remote Sens. 24, 183–188.
Taran, Y.A., 2011. N_2, Ar, and He as a tool for discriminating sources of volcanic fluids with application to Vulcano, Italy. Bull. Volcanol. 73, 395–408.
Tassi, F., Vaselli, O., Papazachos, C.B., Giannini, L., Chiodini, G., Vougioukalakis, G.E., Karagianni, E., Vamvakaris, D., Panagiotopoulos, D., 2013. Geochemical and isotopic changes in the fumarolic and submerged gas discharges during the 2011–2012 unrest at Santorini caldera (Greece). Bull. Volcanol. 75, 711.
Vaselli, O., Tassi, F., Giannini, L., Capaccioni, B., Montegrossi, G., 2006. Sampling and analysis of volcanic gases. Acta Volcanol. 18, 65–76.
Venturi, S., Tassi, F., Vaselli, O., Vougioukalakis, G.E., Rashed, H., Kanellopoulos, C., Caponi, C., Capecchiacci, F., Cabassi, J., Ricci, A., Giannini, L., 2018. Active hydrothermal fluids circulation triggering small-scale collapse events: the case of the 2001–2002 fissure in the Lakki Plain (Nisyros Island, Aegean Sea, Greece). Nat. Hazards 93, 601–626.
Vollmer, R., 1976. Rb-Sr and U-Th-Pb systematics of alkaline rocks: the alkaline rocks from Italy. Geochim. Cosmochim. Acta 40, 283–295.
Warr, O., Sherwood, L.B., Fellowes, J., Sutcliffe, C.N., McDermott, J.M., Holland, G., Mabry, J.C., Ballentine, C.J., 2018. Tracing ancient hydrogeological fracture network age and compartmentalisation using noble gases. Geochim. Cosmochim. Acta 222, 340–362.
Werner, C., Evans, W.C., Poland, M., Tucker, D.S., Doukas, M.P., 2009. Long-term changes in quiescent degassing at Mount Baker Volcano, Washington, USA; Evidence for a stalled intrusion in 1975 and connection to a deep magma source. J. Volcanol. Geoth. Res. 186, 379–386.